Entrainment and growth of vortical disturbances in the channel-entrance region

Pierre Ricco[1]† **and Claudia Alvarenga**[1,2]

[1]Department of Mechanical Engineering, The University of Sheffield, S1 3JD Sheffield, United Kingdom

[2]Department of Fluid Dynamics, A*Star Institute of High Performance Computing, Singapore

(Received xx; revised xx; accepted xx)

Published as Ricco, P. Alvarenga, C. "Entrainment and growth of vortical disturbances in the channel-entrance region", J. Fluid Mech. (2021), vol. 927, A18, doi:10.1017/jfm.2021.765

The entrainment of free-stream unsteady three-dimensional vortical disturbances in the entry region of a channel is studied via matched asymptotic expansions and by numerical means. The interest is in flows at Reynolds numbers where experimental studies have documented the occurrence of intense transient growth, despite the flow being stable according to classical stability analysis. The analytical description of the vortical perturbations at the channel mouth reveals how the oncoming disturbances penetrate into the wall-attached shear layers and amplify downstream. The effects of the channel confinement, the streamwise pressure gradient, and the viscous/inviscid interplay between the oncoming disturbances and the boundary-layer perturbations are discussed. The composite perturbation velocity profiles are employed as initial conditions for the unsteady boundary-region perturbation equations. At a short distance from the channel mouth, the disturbance flow is mostly confined within the shear layers and assumes the form of streamwise-elongated streaks, while farther downstream the viscous disturbances permeate the whole channel although the base flow is still mostly inviscid in the core. Symmetrical disturbances exhibit a more significant growth than anti-symmetrical disturbances, the latter maintaining a nearly constant amplitude for several channel heights downstream before growing transiently, a unique feature not reported in open boundary layers. The disturbances are more intense as the frequency decreases or the bulk Reynolds number increases. We compute the spanwise wavelengths that cause the most intense downstream growth and the threshold wall-normal wavelengths below which the perturbations are damped through viscous dissipation.

Key words:

1. Introduction

Laminar-to-turbulent transition is a phenomenon that has puzzled scientists since the pioneering experimental work of Reynolds (1883). Even in the simplest geometries, it is often not completely clear how the laminar flow becomes unstable and breaks down to turbulence. For example, all theoretical and numerical works show that laminar pipe and Couette flows are always linearly stable at every Reynolds number, whereas obviously

† Email address for correspondence: p.ricco@sheffield.ac.uk

turbulence is ubiquitous in these flows once the Reynolds number becomes large enough. Transition in plane Poiseuille flows is often observed at Reynolds numbers that are smaller than the critical ones predicted by linear stability theory (Drazin & Reid 2004). The problem is relevant from practical and fundamental points of view. In engineering applications, it is paramount to predict how and where transition occurs because most oil and gas channel and pipe flows are turbulent even at moderate flow rates, which impacts on the design of these fluids engineering systems. Given the extraordinary mathematical difficulties that it poses, transition to turbulence is also a topic of fundamental interest per se and has thus attracted enormous attention from researchers of various backgrounds.

Most of the research efforts on the stability of channel and pipe flows have focussed on the fully-developed laminar flow regime, i.e., sufficiently downstream of the entrance where the base flow is independent of the streamwise coordinate and has reached the typical parabolic profile. Much less attention has instead been devoted to developing confined flows in the entrance region, where the base flow evolves along the streamwise direction and the boundary layers over the solid walls grow until they merge once the flow becomes fully developed. The main objective of our work is therefore to investigate the entrainment of vortical disturbances in the entrance region of a pressure-driven incompressible plane channel flow as a cardinal step towards a full comprehension of transition in confined flows.

As the understanding of how outer disturbances penetrate and interact with the boundary layers developing on the channel walls is fundamental for our study, it is instructive to review the state of the art on the response and receptivity of boundary layers to external disturbances (in §1.1) and on the stability and transition of channel entrance flows (in §1.2).

1.1. *Boundary-layer flows*

Laminar-to-turbulent transition in free-stream boundary layers is affected by acoustic, kinematic, or entropic disturbances of the oncoming stream, often referred to as free-stream turbulence. The turbulence level Tu, defined as the root mean square of the intensity of the velocity fluctuations, plays a fundamental role in transition (Dryden 1955). It has become widely accepted that for Tu smaller than about 0.1% transition occurs as a result of the excitation of Tollmien-Schlichting (TS) waves through receptivity, i.e., the mechanism by which disturbances penetrate the boundary layer and become unstable (Goldstein 1983; Ruban 1984, 1985; Goldstein 1985; Reed *et al.* 2015). For Tu larger than about 1%, transition instead occurs earlier and the TS-wave scenario only plays a secondary role. This phenomenon is referred to as bypass transition (Morkovin 1984) and is characterized by the appearance of streamwise-elongated flow structures of low and high speed, first reported by Dryden (1936) and Taylor (1939). These longitudinal streaky structures are nowadays widely referred to as Klebanoff modes (Klebanoff 1971; Kendall 1991). Flow visualizations by Matsubara & Alfredsson (2001) showed that laminar streaks are of low frequency and have a relatively short spanwise wavelength. They eventually break up, leading the flow to the fully-developed turbulent regime. Jacobs & Durbin (2001) simulated bypass transition numerically by prescribing free-stream turbulence as the continuous Orr-Sommerfeld/Squire spectrum, as proposed by Grosch & Salwen (1978), and observed streaks of negative streamwise velocity perturbation upon which turbulent spots start to develop.

A theoretical framework for the interaction between free-stream turbulence and a boundary layer, and specifically the filtering and amplification of low-frequency disturbances by the base-flow shear, was developed by Leib *et al.* (1999) (hereinafter denoted by LWG99). They employed the linearized unsteady boundary region equations (Kemp

1951) to describe the streaks dynamics. These equations are the asymptotic limit of the Navier-Stokes equations for small-amplitude, low-frequency disturbances at high Reynolds numbers. The initial and boundary conditions in LWG99 are unequivocally linked to the oncoming free-stream vortical disturbances. The initial conditions describe the interplay of the free-stream perturbation with the boundary layer in the proximity of the leading edge, while the free-stream boundary conditions model the continuous effect of the outer-flow perturbation on the boundary layer as it evolves downstream. Initial and boundary conditions are related through matched asymptotic expansions, which reveals how the free-stream turbulence links with the boundary layer. LWG99 found that the wall-normal and spanwise velocity components of the outer perturbation play a key role in the creation and development of the boundary-layer streaks.

Based on the work by LWG99, Ricco (2009) computed the second-order terms of the laminar streaks that are dominant in the outer portion of the boundary layer and found good agreement with the experimental data by Westin *et al.* (1994). Using a related mathematical framework, Xu *et al.* (2020) studied the formation of streaks and Görtler vortices in a boundary layer with a pressure gradient. This study was a substantial extension of LWG99's work because the distortion of the free-stream vortical disturbances due to the pressure gradient had to be taken into account.

As the mathematical approach employed by LWG99 and Ricco (2009) takes into account nonparallel effects, streak unsteadiness, spanwise viscous diffusion, and the role of free-stream fluctuations, we therefore use these frameworks to investigate the entrainment of vortical disturbances in the entry region of channel flows, including the effects of confinement and of the base-flow streamwise pressure gradient.

1.2. *Channel-entrance flows*

According to linear stability theory, the fully-developed pipe flow is always linearly stable (Drazin & Reid 2004), whereas the fully-developed channel flow between parallel plates becomes linearly unstable at $R_p = 5772$ (Orszag 1971), where the Reynolds number R_p is based on the half-channel height and the centreline Poiseuille velocity, although in experiments transition has been observed at Reynolds numbers lower than $R_p = 2000$ (Patel & Head 1969; Kao & Park 1970; Nishioka *et al.* 1975; Carlson *et al.* 1982).

Much less attention has been devoted to the entrance flow region, i.e., where the base flow is still developing downstream. The laminar channel entrance flow has been studied by an approximate matching procedure (Schlichting 1934), by composite asymptotic solutions combining the inviscid channel core flow and the viscous boundary layers on the channel walls (Wilson 1970; Van Dyke 1969), by a series expansion in terms of exponential functions (Sparrow *et al.* 1964), and by solving the boundary-layer equations numerically (Bodoia & Osterle 1962). A few experimental works have also been reported, such as Sparrow *et al.* (1967), Beavers *et al.* (1970), and Asai & Floryan (2004), with the last two works being of particular interest as the width-height aspect ratios were 51:1 and 26.7:1 respectively, therefore approximating the ideal channel flow between infinite parallel plates with good accuracy. As the inviscid flow in the channel core accelerates because of the streamwise pressure gradient, the boundary layers on the channel walls are affected by the change in pressure and grow along the so-called entrance region, downstream of which the channel flow is fully influenced by viscous effects and is parallel to the walls.

Linear classical stability analysis of the channel entrance flow has been investigated by employing the parallel-flow assumption (Hahneman *et al.* 1948; Chen & Sparrow 1967; Gupta & Garg 1981*a*,*b*), by including the nonparallel flow effects (Garg & Gupta 1981*a*,*b*), and by using the triple-deck formalism (Smith & Bodonyi 1980). To the best of

our knowledge, no experimental works exist to confirm these theoretical and numerical results. Although discrepancies exist, especially in the computation of the neutral curve arguably because of the different mathematical frameworks adopted, the general consensus is that the critical bulk Reynolds number is smaller at larger downstream distances, which means that, at a fixed bulk Reynolds number, the channel flow is more stable in the entrance region than in the fully-developed region.

Including nonparallel effects, Duck (2005) studied the transient growth in the entrance regions of channel and pipe flows. He introduced the disturbance at the wall by suction and blowing or by feeding the boundary layers near the inlet with the boundary-layer eigensolution discovered by Luchini (1996). Buffat *et al.* (2014) performed direct numerical simulations of bypass transition in developing channel flows. They induced transition through the optimal disturbances of Andersson *et al.* (1999) and Luchini (2000) confined within the upper-wall boundary layer, thus mimicking the disturbances induced by distributed obstacles. They reported the generation of streaks, their subsequent transient growth, and the eventual flow breakdown caused by the interaction between the upper and lower boundary layers. More recently, Alizard *et al.* (2018) studied the problem of laminar-to-turbulent transition of a channel entrance flow subject to optimal wavepackets as initial conditions. Transition was found to be triggered by the secondary instability of the streaky structures forming within the boundary layers.

Despite these research efforts, the physical mechanisms by which free-stream vortical disturbances superpose on the oncoming inviscid flow, approach the channel entrance, entrain in the channel mouth, penetrate the boundary layers attached on the channel walls, and amplify downstream are still unknown as they have never been studied. These phenomena represent the response problem to external disturbances, which has been studied quite extensively in the context of open boundary layers (Dietz 1999; Leib *et al.* 1999; Wu 2001; Wundrow & Goldstein 2001; Ricco *et al.* 2011) and is well recognised as fundamental for the understanding of transition to turbulence. The sensitivity of entrance flows to the free-stream disturbances entrained in the confined region and their influence on the downstream breakdown to turbulence has first been noticed by Osborne Reynolds in his pioneering work on transition in pipe flow (Reynolds 1883). In his search for a critical velocity above which transition would occur, Reynolds states:"...if there were a critical velocity at which, for any disturbance whatever, the water became stable, this velocity was much less, than that at which it would become unstable for infinitely small disturbances...". Davies & White (1928) further remark:"There can be little doubt that the primary cause is disturbance at inlet to the pipe, but the manner in which such disturbance increases the resistance in the test length is not altogether clear." Experiments on channel entrance flows by Zanoun *et al.* (2009) and Nishioka & Asai (1985), and the direct numerical simulations of an entrance pipe flow by Wu *et al.* (2015) further confirm the significant influence of the intensity, frequency, and azimuthal location of the inlet vortical perturbations.

1.3. *Objectives*

In this paper we report a mathematical and numerical analysis of the response of the channel-flow entrance flow to gust-type vortical disturbances occurring in the inviscid core of the inlet flow. We have been motivated by the fact that, in none of the previous theoretical and numerical studies on the channel entrance flow, realistic physical disturbances known to amplify and cause bypass transition have been prescribed at the channel mouth.

We formulate the theory under the reasonable assumptions of high Reynolds number and of vortical disturbances of small amplitude and low frequency. The latter assumption

is adopted because low-frequency perturbations have been shown to be the most likely to penetrate shear layers and amplify downstream to cause transition (Matsubara & Alfredsson 2001). We are particularly interested in explaining how the disturbances evolve from the inlet, penetrate into the boundary layers, and grow within the channel. We study how the perturbation dynamics depends on the flow parameters, such as the frequency and wavelengths of the entrained disturbance. We believe that this mathematical approach affords a robust basis for the understanding of the relationship between the transitional Reynolds number and the role of entrained turbulence in laminar-to-turbulent transition in channel flows. Our analysis is restricted to linearized dynamics under the assumption of small perturbations, and we are currently extending our framework to the nonlinear case.

In §2, the scaling and assumptions are presented, together with the governing equations and the numerical procedures. The initial development of the perturbation flow is studied in §3 and the downstream perturbation flow dynamics is discussed in §4. The Supplementary Material §S1 and §S2 present the initial and downstream base-flow dynamics.

2. Scaling and equations of motion

In this section, we first present the asymptotic scaling in §2.1 and the equations of motion in §2.2. In §2.3 we discuss how the linear stability results obtained by Gupta & Garg (1981*a*), Garg & Gupta (1981*a*), and Garg & Gupta (1981*b*) are useful to extract the critical streamwise location downstream of which exponentially-growing waves may occur, and we describe the numerical procedures in the Supplementary Material §2.4.

2.1. *Scaling and asymptotic regions*

We consider the pressure-driven incompressible flow at the entrance of a channel confined between two infinite parallel plates. Dimensional quantities are hereafter indicated by the superscript $*$. As the oncoming uniform flow of velocity U^*_∞ enters the channel, two boundary layers develop on the walls. The thickness of these viscous layers increases downstream until they merge and the channel flow becomes fully viscous. The flow is described by a Cartesian coordinate system, that is, by a position vector $\mathbf{x} = x^*\hat{\mathbf{i}} + y^*\hat{\mathbf{j}} + z^*\hat{\mathbf{k}}$, where x^*, y^*, and z^* represent the streamwise, wall-normal, and spanwise directions, respectively. The channel walls are at $y^* = 0$ and $y^* = 2h^*$, where h^* is the half-channel height. Lengths are scaled by a reference length λ^*, specified below. Superimposed on U^*_∞ are gust-type vortical fluctuations advected by the base flow. A difference from the free-stream boundary-layer case studied by LWG99 is that we only consider free-stream disturbances with a maximum wall-normal wavelength $\lambda_{y,max} = 2h$ and with $2h/\lambda_y \in \mathbb{Z} > 0$ to preserve symmetries between the two channel halves. Velocities are normalized by U^*_∞, the pressure is scaled by $\rho^* U^{*2}_\infty$, where ρ^* is the density of the fluid, and the time is scaled by λ^*/U^*_∞. The vorticity fluctuations at streamwise locations sufficiently near $x = 0$ and sufficiently far from the channel walls can be expressed mathematically as a pair of vortical disturbances with equal and opposite wall-normal wavenumbers $\pm k^*_y$,

$$\mathbf{u} = \hat{\mathbf{i}} + \varepsilon \mathbf{u}_\infty(x - t, y, z) = \hat{\mathbf{i}} + \varepsilon(\hat{\mathbf{u}}^\infty_+ e^{ik_y y} + \hat{\mathbf{u}}^\infty_- e^{-ik_y y}) e^{i(k_x x + k_z z - k_x t)} + \text{c.c.}, \qquad (2.1)$$

where c.c. stands for the complex conjugate, $\varepsilon \ll 1$ is the amplitude of the gust, and $\hat{\mathbf{u}}^\infty_\pm = \{\hat{u}^\infty_{x\pm}, \hat{u}^\infty_{y\pm}, \hat{u}^\infty_{z\pm}\}$, where $\hat{u}^\infty_{x\pm,y\pm,z\pm} = \mathcal{O}(1)$ are complex quantities. The reference length is $\lambda^* = \lambda^*_z$ ($k_z = 2\pi$), the spanwise wavelength of the gust. The simple form

of vortical disturbances given in (2.1) is assumed for mathematical simplicity. The formulation can be generalized to realistic disturbances consisting of a superposition of different gust disturbances (Zhang *et al.* 2011). A similar choice for the oncoming disturbance was employed for the free-stream boundary-layer cases studied by Ricco *et al.* (2011) and Marensi *et al.* (2017), who prescribed the vorticity fluctuations as a pair of gust disturbances with equal and opposite spanwise wavenumbers. Disturbances (2.1) are physically realistic because they may be generated, for example, by a vibrating ribbon at the channel mouth, as performed by Dietz (1999) in his seminal experimental study of boundary-layer receptivity to two-dimensional free-stream disturbances, or more recently by Borodulin *et al.* (2021*a*,*b*) for the case of three-dimensional free-stream disturbances. The special cases $\hat{u}^\infty_{x+} = \pm\hat{u}^\infty_{x-} \in \mathbb{R}$ are of interest in our work. The case $\hat{u}^\infty_{x+} = \hat{u}^\infty_{x-}$ leads to a streamwise velocity that is symmetric with respect to the centreline, while the case $\hat{u}^\infty_{x+} = -\hat{u}^\infty_{x-}$ produces an antisymmetric streamwise velocity. In the first case, we take $\hat{u}^\infty_{z+} = \hat{u}^\infty_{z-} \in \mathbb{R}$ and in the second case we take $\hat{u}^\infty_{z+} = -\hat{u}^\infty_{z-} \in \mathbb{R}$. The continuity equation for the gust disturbance is expressed as

$$k_x\hat{u}^\infty_{x\pm} \pm k_y\hat{u}^\infty_{y\pm} + k_z\hat{u}^\infty_{z\pm} = 0, \tag{2.2}$$

which fixes $\hat{u}^\infty_{y\pm}$ once the other quantities are known. The focus is on low-frequency (i.e., long-wavelength) disturbances with a streamwise wavenumber $k_x = 2\pi\lambda^*_z/\lambda^*_x \ll 1$, where λ^*_x is the streamwise wavelength of the gust, as these perturbations are able to penetrate a boundary layer and generate the laminar streaks (Matsubara & Alfredsson 2001). The free-stream flow thus assumes the symmetric and anti-symmetric forms:

Symmetric

$$u_x = 1 + 4\varepsilon\hat{u}^\infty_{x+}\cos(k_y y)\cos(k_x x + k_z z - k_x t), \tag{2.3a}$$

$$u_y = \frac{4\varepsilon k_z\hat{u}^\infty_{z+}}{k_y}\sin(k_y y)\sin(k_x x + k_z z - k_x t), \tag{2.3b}$$

$$u_z = 4\varepsilon\hat{u}^\infty_{z+}\cos(k_y y)\cos(k_x x + k_z z - k_x t), \tag{2.3c}$$

and

Anti-symmetric

$$u_x = 1 - 4\varepsilon\hat{u}^\infty_{x+}\sin(k_y y)\sin(k_x x + k_z z - k_x t), \tag{2.4a}$$

$$u_y = -\frac{4\varepsilon k_z\hat{u}^\infty_{z+}}{k_y}\cos(k_y y)\cos(k_x x + k_z z - k_x t), \tag{2.4b}$$

$$u_z = -4\varepsilon\hat{u}^\infty_{z+}\sin(k_y y)\sin(k_x x + k_z z - k_x t). \tag{2.4c}$$

The wall-normal velocity components have therefore opposite symmetries with respect to the streamwise and spanwise velocity components, as also shown by Gustavsson (1991). The Reynolds number is defined as

$$R_\lambda = \frac{U^*_\infty\lambda^*_z}{\nu^*}, \tag{2.5}$$

and is assumed to be asymptotically large, i.e., $R_\lambda \gg 1$. Inside the channel, the disturbances evolve downstream on a length scale that is comparable with the streamwise wavelength of the gust. Hence, a distinguished scaling for the streamwise direction is $k_x = \mathcal{O}(R_\lambda^{-1})$ or $\overline{x} = k_x x = 2\pi x^*/\lambda^*_x = \mathcal{O}(1)$. The disparity between the streamwise and spanwise scales implies that disturbances of amplitude $\mathcal{O}(\varepsilon)$ may generate streamwise velocity perturbations with an amplitude of $\mathcal{O}(\varepsilon/k_x)$ in the viscous layers. These amplitudes are assumed to be much smaller than the amplitude of the base flow, which

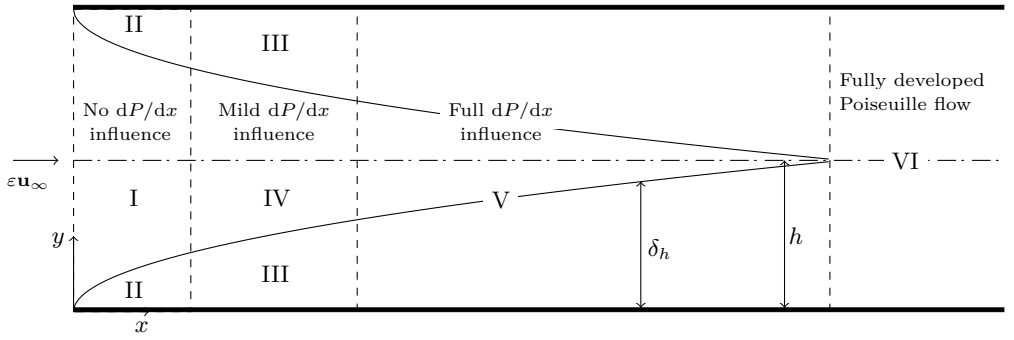

Figure 1: Asymptotic regions of the channel flow (not in scale). The boundary-layer thickness δ_h is defined in the Supplementary Material §S2.

translates to $\varepsilon/k_x \ll 1$ or $\varepsilon R_\lambda \ll 1$ and implies that the Navier-Stokes equations may be linearized.

As shown in figure 1, the flow domain is divided into six asymptotic regions. Regions I and II pertain to the part of the channel where both the base flow and the perturbation flow are influenced by the confinement of the channel but the effect of the base-flow streamwise pressure gradient is negligible because of the small downstream distance. Regions III and IV are fully affected by the channel confinement, but the effect of the streamwise pressure gradient is mild in region IV and negligible in region III. In region V, the effects of confinement and pressure gradient are influential, but the base flow has not reached the fully-developed Poiseuille profile. In region VI, the base flow is fully developed.

Region I is located at a $x = \mathcal{O}(1)$ distance from the inlet and extends along the whole wall-normal direction. The base and the perturbation flows are both inviscid there and the flow field can be adequately described by rapid distortion theory (Hunt 1973; Goldstein 1978). The solution is expressed in terms of a velocity potential and the presence of the lower and upper plates is taken into account through the specification of appropriate boundary conditions obtained by asymptotic matching with the wall-normal velocity component of the boundary-layer disturbance. Region II is a viscous region underneath region I, where the boundary-layer thickness is much smaller than the spanwise wavelength, i.e., $\delta^*/\lambda_z^* \ll 1$. This limit allows neglecting the spanwise viscous terms in the spanwise momentum equation because they are much smaller than the wall-normal viscous terms. The combined flow of regions I and II is studied in §3.1.

Downstream of region II the boundary-layer thickness and the spanwise wavelength of the disturbance become of the same order, i.e., $\lambda_z^*/\delta^* = \mathcal{O}(1)$, and thus the wall-normal and spanwise viscous terms are of comparable magnitude. This viscous region is named region III, where $\overline{x} = \mathcal{O}(1)$ and the flow is governed by the Linear Unsteady Boundary Region (LUBR) equations, that is the rigorous asymptotic limit of the Navier-Stokes equations for long-wavelength/low-frequency disturbances (Leib *et al.* 1999). We assume that the base flow in regions II and III is of the Blasius type, hence the base-flow pressure gradient effect is negligible. Regions II and III occur in both boundary layers developing on the two channel walls. Region IV is the asymptotic region between the two regions III. Here, the base flow is inviscid, while the perturbation flow is viscous and influenced by the increased boundary-layer thickness and by the confinement of the channel flow. The pressure gradient only has a second-order effect. The combined flow of regions III and IV is discussed briefly in §3.2.

The region of main interest is region V, where the flow is fully influenced by the channel confinement and the base-flow streamwise pressure gradient. It extends from the lower to the upper wall of regions III and IV. In region V, differently from region III where the Blasius solution applies, the base flow is not self-similar because of the unknown base-flow pressure gradient and nonparallel effects as the base-flow wall-normal velocity plays a key role. The latter vanishes further downstream in the fully-developed region VI, where the parabolic Poiseuille profile occurs.

2.2. *Governing equations and boundary conditions*

The flow field is governed by the non-dimensional incompressible continuity and Navier-Stokes equations,

$$\nabla \cdot \mathbf{u} = 0 \tag{2.6}$$

$$\frac{\partial \mathbf{u}}{\partial t} + (\mathbf{u} \cdot \nabla)\,\mathbf{u} = -\nabla p + \frac{1}{R_\lambda}\nabla^2 \mathbf{u}. \tag{2.7}$$

The velocity $\mathbf{u}$ and the pressure p are expressed as the superposition of the base-flow velocity $\overline{\mathbf{U}}(\overline{x}, y)$ and pressure $\overline{P}(\overline{x}) = \mathcal{O}(1)$ and the perturbation flow $\{\mathbf{u}', p'\} = \{u', v', w', p'\}$ as follows

$$\{\mathbf{u}, p\} = \underbrace{\begin{pmatrix} U(\overline{x}, y) \\ k_x V(\overline{x}, y) \\ 0 \\ P(\overline{x}) \end{pmatrix}}_{\overline{\mathbf{U}},\, \overline{P}} + \varepsilon \underbrace{\begin{pmatrix} \overline{u}_0(\overline{x}, y) \\ \overline{v}_0(\overline{x}, y) \\ \overline{w}_0(\overline{x}, y) \\ \overline{p}_0(\overline{x}, y) \end{pmatrix} e^{i(k_z z - k_x t)}}_{\mathbf{u}',\, p'} + \text{c.c.}, \tag{2.8}$$

and

$$\{\overline{u}_0, \overline{v}_0\} = \left\{\overline{u}^{(0)}, k_x \overline{v}^{(0)}\right\} + \left\{\frac{ik_z}{k_x}\overline{u}, ik_z \overline{v}\right\}, \tag{2.9a}$$

$$\overline{w}_0 = -\frac{ik_x}{k_z}\overline{w}^{(0)} + \overline{w}, \tag{2.9b}$$

$$\overline{p}_0 = \frac{k_x}{R_\lambda}\overline{p}^{(0)} + \frac{ik_z}{R_\lambda}\overline{p}. \tag{2.9c}$$

Note that the main difference between $\overline{v}$ and $\overline{v}^{(0)}$ and the corresponding components in (4.1) on page 176 of LWG99 is the missing factor $(2\overline{x})^{1/2}$ in (2.8), which arises in LWG99's case because of the Blasius-similarity scaling. Substituting (2.8) into equations (2.6)-(2.7) and collecting the terms of $\mathcal{O}(1)$ yields the base-flow boundary-layer equations,

$$\frac{\partial U}{\partial \overline{x}} + \frac{\partial V}{\partial y} = 0, \tag{2.10}$$

$$U\frac{\partial U}{\partial \overline{x}} + V\frac{\partial U}{\partial y} = -\frac{\mathrm{d}P}{\mathrm{d}\overline{x}} + \frac{1}{\mathcal{F}}\frac{\partial^2 U}{\partial y^2}, \tag{2.11}$$

$$\frac{\partial P}{\partial y} = 0, \tag{2.12}$$

for $k_x, R_\lambda^{-1} \ll 1$ and $\mathcal{F} = k_x R_\lambda = \mathcal{O}(1)$. The pressure P must be solved for, unlike simpler free-stream boundary-layer cases where the imposed pressure gradient is known. By exploiting the symmetry over the two channel halves, equations (2.10) and (2.11) are solved in the bottom half of the channel together with the integral form of the continuity

equation,

$$\frac{1}{h}\int_0^h U\mathrm{d}y = 1, \tag{2.13}$$

and are subject to the no-slip and no-penetration conditions at the wall,

$$U = V = 0 \quad \text{at} \quad y = 0, \tag{2.14}$$

and to the symmetry conditions at the centreline

$$\frac{\partial U}{\partial y} = V = 0 \quad \text{at} \quad y = h. \tag{2.15}$$

It must be noted that, although the boundary-layer approximation is adopted in the limit $R_\lambda^{-1} \to 0$, i.e., the streamwise viscous diffusion and the wall-normal pressure gradient are negligible, the flow is solved along the whole channel height. Other boundary-layer approximations, such as Schlichting (1934) and Collins & Schowalter (1962), instead split the channel domain in the near-wall regions and in the inner core.

A standard manipulation of the Navier-Stokes and continuity equations is carried out to obtain the equations of the perturbation flow. Because the perturbation pressure p' at the wall is unknown, it is common practice to eliminate the pressure from (2.6)-(2.7) by reducing them to a fourth-degree equation for the wall-normal velocity and a second-degree equation for the wall-normal vorticity (Kim *et al.* 1987; Schmid & Henningson 2001). Using the compact notation of Kim *et al.* (1987), these equations read

$$\frac{\partial}{\partial t}\nabla^2 v = h_v + \frac{1}{R_\lambda}\nabla^4 v, \tag{2.16}$$

$$\frac{\partial \omega_y}{\partial t} = h_{\omega_y} + \frac{1}{R_\lambda}\nabla^2 \omega_y, \tag{2.17}$$

where

$$h_v = -\frac{\partial}{\partial y}\left(\frac{\partial H_x}{\partial x} + \frac{\partial H_z}{\partial z}\right) + \left(\frac{\partial^2}{\partial x^2} + \frac{\partial^2}{\partial z^2}\right) H_y, \qquad h_{\omega_y} = \frac{\partial H_x}{\partial z} - \frac{\partial H_z}{\partial x}, \tag{2.18}$$

and

$$H_j = -\left(u\frac{\partial u_j}{\partial x} + v\frac{\partial u_j}{\partial y} + w\frac{\partial u_j}{\partial z}\right), \tag{2.19}$$

where the subscript $j = x, y, z$ indicates the velocity component along the denoted coordinate. The wall-normal vorticity perturbation is

$$\omega_y' = \left[\frac{(ik_z)^2}{k_x}\overline{u} - k_x\frac{\partial \overline{w}}{\partial \overline{x}}\right] e^{i(k_z z - k_x t)} + \text{c.c.} = -\frac{k_z^2}{k_x}\overline{u}e^{i(k_z z - k_x t)} + \mathcal{O}(k_x) + \text{c.c.} \tag{2.20}$$

As the perturbation is elongated in the streamwise direction, vorticity is mostly created by the streamwise velocity perturbation $\overline{u}$ and the contribution of the spanwise velocity $\overline{w}$ can be neglected. The equations of motion for the perturbation flow are derived by substituting (2.8) and (2.9) into (2.16) and (2.17), using (2.20), and collecting terms of

$\mathcal{O}(\varepsilon)$ for $k_x, R_\lambda^{-1} \ll 1$ and $\mathcal{F} = \mathcal{O}(1)$. They read

$$\left(ik_z^2 - \frac{k_z^4}{\mathcal{F}} - k_z^2\frac{\partial V}{\partial y} + \frac{\partial^3 V}{\partial y^3}\right)\overline{v} - \left(k_z^2 V - \frac{\partial^2 V}{\partial y^2}\right)\frac{\partial \overline{v}}{\partial y} + \left(-i + \frac{2k_z^2}{\mathcal{F}} + \frac{\partial V}{\partial y}\right)\frac{\partial^2 \overline{v}}{\partial y^2} + V\frac{\partial^3 \overline{v}}{\partial y^3} + U\frac{\partial^3 \overline{v}}{\partial \overline{x}\partial y^2} - \frac{1}{\mathcal{F}}\frac{\partial^4 \overline{v}}{\partial y^4} - \left(k_z^2 U + \frac{\partial^2 U}{\partial y^2}\right)\frac{\partial \overline{v}}{\partial \overline{x}} - \left(k_z^2\frac{\partial V}{\partial \overline{x}} - \frac{\partial^3 V}{\partial \overline{x}\partial y^2}\right)\overline{u} - 2\frac{\partial^2 U}{\partial \overline{x}\partial y}\frac{\partial \overline{u}}{\partial \overline{x}} - 2\frac{\partial U}{\partial \overline{x}}\frac{\partial^2 \overline{u}}{\partial \overline{x}\partial y} - \frac{\partial V}{\partial \overline{x}}\frac{\partial^2 \overline{u}}{\partial y^2} = 0, \tag{2.21}$$

$$\left(-i + \frac{k_z^2}{\mathcal{F}} + \frac{\partial U}{\partial \overline{x}}\right)\overline{u} + V\frac{\partial \overline{u}}{\partial y} + U\frac{\partial \overline{u}}{\partial \overline{x}} - \frac{1}{\mathcal{F}}\frac{\partial^2 \overline{u}}{\partial y^2} + \frac{\partial U}{\partial y}\overline{v} = 0. \tag{2.22}$$

Equations (2.21) and (2.22) are also satisfied by $\{\overline{u}^{(0)}, \overline{v}^{(0)}\}$. Equation (2.22) is the LUBR x-momentum equation as a consequence of (2.20). It is immediately clear from (2.21) and (2.22) that the most significant difference between the perturbation dynamics in the entrance region and in the fully-developed Poiseuille-flow region further downstream lies in the presence of $\overline{u}$ and $\overline{v}$ in both equations in the entry-flow case, thus producing two-way coupling. When the flow is instead fully developed, $\partial U/\partial \overline{x}$ and V are null and therefore, like in the Orr-Sommerfeld equation describing the classical linear stability, equation (2.21) can be solved by itself to find the wall-normal velocity, which then drives the streamwise disturbance through the lift-up term $\overline{v}\partial U/\partial y$ in the vorticity equation (Schmid & Henningson 2001).

Equations (2.21) and (2.22) are solved numerically subject to

$$\overline{u} = \overline{v} = \frac{\partial \overline{v}}{\partial y} = 0 \tag{2.23}$$

at $y = 0$ and $y = 2h$. The spanwise velocity component $\overline{w}$ is computed a posteriori from the continuity equation,

$$\overline{w} = -\left(\frac{\partial \overline{u}}{\partial \overline{x}} + \frac{\partial \overline{v}}{\partial y}\right). \tag{2.24}$$

The pressure is computed a posteriori by substituting (2.8) into the spanwise momentum equation and collecting terms of $\mathcal{O}(\varepsilon)$,

$$\overline{p} = \frac{\mathcal{F}}{k_z^2}\left[\left(-i + \frac{k_z^2}{\mathcal{F}}\right)\overline{w} + U\frac{\partial \overline{w}}{\partial \overline{x}} + V\frac{\partial \overline{w}}{\partial y} - \frac{1}{\mathcal{F}}\frac{\partial^2 \overline{w}}{\partial y^2}\right]. \tag{2.25}$$

The base-flow equations (2.10) and (2.11) and the LUBR equations (2.21) and (2.22) are parabolic and thus solved through a downstream marching procedure. The specification of the appropriate initial conditions is of crucial importance. We have thus devoted great attention to the formulation of physically meaningful initial conditions for both the base and the perturbation flows. The initial base-flow velocity profile has usually been assumed uniform (Bodoia & Osterle 1962; Van Dyke 1969; Wilson 1970). We instead take into account the interaction between the oncoming flow and the channel walls by deriving an asymptotic solution composed of the Blasius flow near the walls (inner solution) and the inviscid flow in the channel core that is distorted by the developing boundary layers (outer solution). A similar approach was employed by Rubin *et al.* (1977). The small-x base-flow asymptotic initial condition used to solve the base-flow equations (2.10) and (2.11) is described in §S1.1.

Perturbation-flow inflow conditions for open boundary-layer computations are often specified as the continuous spectrum of the Orr-Sommerfeld/Squire equations (Jacobs &

Durbin 2001; Brandt *et al.* 2004) or by selecting optimal perturbations, as those obtained for the flat plate case by Andersson *et al.* (1999) and Luchini (2000). As inflow conditions, Buffat *et al.* (2014) imposed optimal disturbances within one of the boundary layers near the channel entrance, while perturbations were absent in the inviscid core. However, as also discussed in the Introduction (refer also to Ricco *et al.* (2016)), neither the continuous spectrum of the Orr-Sommerfeld/Squire equations nor the optimal perturbations have to date been proven to be physically realizable perturbations that can be used as inflow conditions.

We instead prescribe initial conditions that are superposed on the inviscid core flow and are fully consistent with the oncoming vortical disturbances at $\overline{x} = 0$, given in (2.1). Like the base flow, these initial conditions are expressed as asymptotic composite solutions of a viscous inner solution within the boundary layer and an outer solution where the base flow is inviscid in the channel core. We do not use optimal perturbations as they are the output of an optimization procedure where the streamwise and spanwise velocities vanish in the inviscid core flow outside of the boundary layer, while we are interested in their entrainment of vortical disturbances that occupy the entire cross-plane at the channel mouth. The initial condition is not imposed at $\overline{x} = 0$ because the wall-normal base-flow velocity is singular there and because the flow field is governed by the full Navier-Stokes equations in the immediate surroundings of the channel mouth. Therefore, the initial conditions are imposed at a location $0 < \overline{x}_0 \ll 1$.

Section 3.1 presents results for the development of the perturbation flow at small-x locations where the base-flow pressure gradient is negligible. These flow fields are small-x asymptotic solutions of the flow in region V and can therefore be used as initial conditions to solve equations (2.21) and (2.22) along the channel, where the base-flow streamwise pressure gradient is fully influential.

2.3. *Critical streamwise location for linear stability*

As we focus on the transient growth of vortical disturbances in the entrance region, a first step is to report, as a function of the Reynolds number, the streamwise distance upstream of which TS-waves do not appear. Garg & Gupta (1981*a*) extended their classical spatial stability study in Gupta & Garg (1981*a*) and Garg & Gupta (1981*b*) to include the nonparallel base-flow effects. The main result is that the entrance flow is always more linearly stable than the fully-developed flow at the same bulk Reynolds number. Figure 2 shows Garg & Gupta (1981*a*)'s computed neutral stability location x_c/h as a function of the Reynolds number $R_h = hR_\lambda = U^*_\infty h^*/\nu^*$ (black circles). The channel flow is stable according to classical stability theory (absence of TS-waves) to the left of the black circles. For $R_h < 3848$, which corresponds to the classical stability Reynolds number $R_p = U^*_p h^*/\nu^* = 3R_h/2 = 5772$, where U^*_p is the maximum velocity of the parabolic Poiseuille profile, the flow is stable at any streamwise location. At $R_h = 3848$ the flow is linearly unstable downstream of $x_c/h \approx 1000$, that is, where it has reached the Poiseuille profile. As R_h increases further, the entrance flow becomes unstable at decreasing streamwise locations. The solid line denotes the end of the entry laminar flow region according to our adopted definition based on the second derivative of the base-flow velocity at the centerline (refer to the Supplementary Material §S2).

We focus on Reynolds numbers in the range $1000 < R_h < 3500$ (marked by the light grey area in figure 2), i.e., small enough for TS-waves not to appear and large enough for algebraically growing perturbations or transition to turbulence to have been observed in experimental studies. Patel & Head (1969)'s air channel experiments, which are particularly relevant because the entrance flow was defined as "sufficiently disturbed", show that intermittency is absent for $R_h < 675$ and the flow is turbulent for $R_h >$

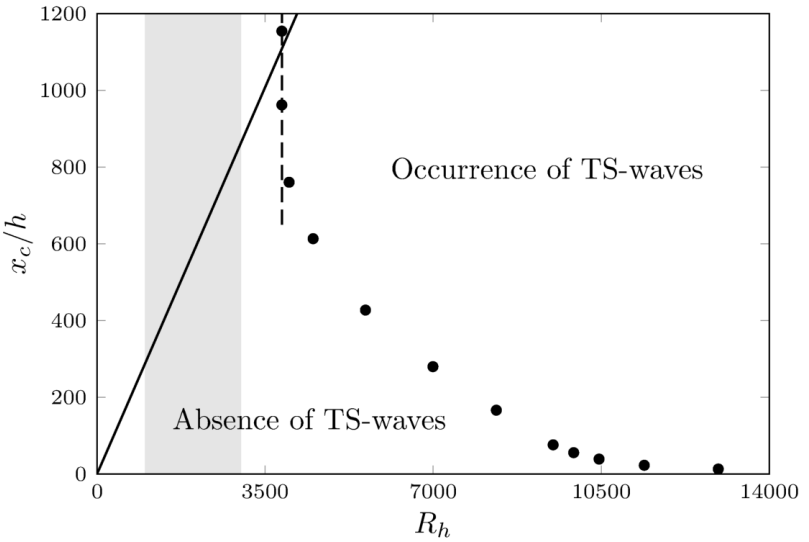

Figure 2: Black circles: streamwise location downstream of which the channel entrance flow becomes unstable according to classical stability theory, i.e., TS-waves start to grow. The data points have been rescaled from the original ones by Garg & Gupta (1981*a*). The dashed line denotes the critical Reynolds number $R_h = 3848$ for the fully-developed Poiseuille flow. Solid black line: end location of the entry laminar channel flow region, according to our definition based on the second derivative of the base-flow velocity at the centerline, as discussed in the Supplementary Material §S2. The grey area illustrates the range of Reynolds numbers for the flows studied in our work.

1250. Kao & Park (1970) report that no instabilities were detected for $R_h < 1250$ in a water channel and Nishioka *et al.* (1975) measured subcritical instabilities triggered by a vibrating ribbon at their lowest $R_h = 2000$. Carlson *et al.* (1982) later found transition in a channel at $R_h = 1000$ and Nishioka & Asai (1985) concluded that no sustained turbulence exists for $R_h < 667$ by observing the decay of large disturbances from the channel inlet.

2.4. *Numerical procedures*

The base-flow continuity and boundary-layer equations (2.10) and (2.11), supplemented by the integral form of the continuity equation (2.13), are discretized according to a scheme that is an improved version of that used by Bodoia & Osterle (1962), whereby (2.13) is integrated using the trapezoidal rule. The base-flow streamwise velocity and pressure fields are computed simultaneously and the base-flow wall-normal velocity is computed a posteriori through the continuity equation. A difference from Bodoia & Osterle (1962) regards the treatment of the nonlinear convective terms in the base-flow x-momentum equation (2.11). In their paper, these terms are linearized, i.e., the values at the previous x locations are used in the nonlinear terms. Here, we instead use a predictor-corrector method for the computation of the convective terms at step n. In the predictor step $n-1$, an initial approximation of the streamwise velocity and pressure fields is calculated via the linearized discrete equations as in Bodoia & Osterle (1962). In the corrector step, new values of U^n and P^n are computed, using U^{n-1} and P^{n-1} in the discretization of the convective terms instead of those at the previous streamwise location. This procedure is repeated iteratively until convergence is

reached. The convergence criterion is based on the wall-normal velocity gradient at the wall, $\partial U/\partial y|_{y=0}$. The asymptotic composite solution of the base flow derived in the the Supplementary Material §S1 is used as initial condition at small $\overline{x}$ values.

The LUBR equations (2.21) and (2.22) are discretized using backward and central finite-difference schemes in $\overline{x}$ and y, respectively. The degree of the wall-normal velocity equation (2.21) is reduced from fourth to second by defining the wall-normal second derivative of $\overline{v}$ as a new variable. The resulting system is written in the form of a block tridiagonal matrix and solved at each $\overline{x}$ by the Thomas algorithm (Cebeci 2002). The asymptotic composite solution given in §3.1 is used as initial condition at small $\overline{x}$ values.

3. Flow development in regions I, II, III, and IV

In this section we discuss the theoretical and numerical results of the base and perturbation flows near the channel entrance, where the effect of the channel confinement plays a leading role, but the influence of the base-flow pressure gradient is negligible at leading order. This mathematical analysis is important because, through the asymptotic formulation, the physical flow features near the entrance are revealed and the flow evolution further downstream inside the channel can be computed. As explained at the end of §2, the results obtained in this section will indeed specify the appropriate initial conditions for the computation of the base and the perturbation flows in region V, where the dynamics is fully influenced by the streamwise pressure gradient. The development of the base flow in regions I and II is presented in the Supplementary Material §S1.

The precise specification of the flow at the channel entrance is relevant as our interest lies in the mathematical description of the inlet profiles to start the computations and to understand how the vortical disturbances are entrained in the channel mouth and how they evolve in the entrance region. The initial development of the perturbation flow, i.e., where the flow is fully influenced by the channel confinement and only mildly by the base-flow streamwise pressure, is studied via matched asymptotic expansions. Asymptotic composite solutions are derived for regions I and II in §3.1 and for regions III and IV in §3.2.

3.1. *Perturbation flow in regions I and II*

All the composite solutions in this section pertain to the lower channel half and symmetries are used to find the quantities in the upper channel half.

In region I the base flow is uniform and inviscid, the perturbation flow is inviscid, and $\overline{x} \ll 1$ with $\mathcal{F} = k_x R_\lambda = \mathcal{O}(1)$. The flow field can thus be adequately described by rapid distortion theory (Goldstein 1978). The velocity is expressed as

$$\begin{aligned} \mathbf{u}_{out} =& \hat{\mathbf{i}} + \varepsilon \left[\mathbf{u}^{(1)}(\overline{x}, y) + k_x \mathbf{u}_1^{(1)}(\overline{x}, y) \right] e^{i(k_z z - k_x t])} + \text{c.c.} \\ =& \hat{\mathbf{i}} + \varepsilon \left(\mathbf{u}_\infty + \nabla\phi + k_x \nabla\phi_1 \right) + \text{c.c.}. \end{aligned} \tag{3.1}$$

The velocity $\mathbf{u}^{(1)}$ is due to the interaction of the free-stream gust (2.1) with the channel walls, while $\mathbf{u}_1^{(1)}$ is generated by the wall-normal boundary-layer perturbation velocity via the gradient $\nabla\phi_1$. The perturbation potential ϕ satisfies the Laplace's equation

$$\nabla^2 \phi = 0, \tag{3.2}$$

subject to

$$\frac{\partial \phi}{\partial y} + u_{\infty y} = 0 \qquad \text{at} \qquad y = 0, 2h, \quad x > 0, \tag{3.3}$$

where $u_{\infty y}(y=0,2h) = \left(\hat{u}^{\infty}_{y+} + \hat{u}^{\infty}_{y-}\right)\exp\left[i(k_x x + k_z z - k_x t)\right]$ is the gust wall-normal velocity found from (2.1) as the channel walls are approached. Expressions (3.3) are the no-penetration boundary conditions at the walls for the wall-normal velocity. To solve (3.2) in the infinite strip $-\infty<x<\infty$, $0\leqslant y\leqslant 2h$, one needs boundary conditions at $y=0,2h$ for $x<0$, which are unknown. However, the interest is in the solution for $x \gg 1$, found by separation of variables,

$$\phi = \frac{\hat{u}^{\infty}_{y+} + \hat{u}^{\infty}_{y-}}{\gamma\left(e^{2\gamma h} - e^{-2\gamma h}\right)}\left[\left(e^{-2\gamma h}-1\right)e^{\gamma y} + \left(e^{2\gamma h}-1\right)e^{-\gamma y}\right]e^{i[k_x(x-t)+k_z z]}, \tag{3.4}$$

where $\gamma = \sqrt{k_x^2 + k_z^2}$. The velocity components of $\mathbf{u}^{(1)} = \left\{u_x^{(1)}, u_y^{(1)}, u_z^{(1)}\right\}$ in (3.1) are

$$\begin{aligned} u_m^{(1)}(\overline{x},y) =& \frac{ik_m e^{i\overline{x}}(\hat{u}^{\infty}_{y+} + \hat{u}^{\infty}_{y-})}{\gamma\left(e^{2\gamma h} - e^{-2\gamma h}\right)}\left[\left(e^{-2\gamma h}-1\right)e^{\gamma y} + \left(e^{2\gamma h}-1\right)e^{-\gamma y}\right] + \\ & \hat{u}^{\infty}_{m+}e^{i\overline{x}+ik_y y} + \hat{u}^{\infty}_{m-}e^{i\overline{x}-ik_y y}, \end{aligned} \tag{3.5}$$

for $m = x, z$ and

$$\begin{aligned} u_y^{(1)}(\overline{x},y) =& \frac{(\hat{u}^{\infty}_{y+} + \hat{u}^{\infty}_{y-})e^{i\overline{x}}}{e^{2\gamma h} - e^{-2\gamma h}}\left[(e^{-2\gamma h}-1)e^{\gamma y} + (1-e^{2\gamma h})e^{-\gamma y}\right] + \\ & \hat{u}^{\infty}_{y+}e^{i\overline{x}+ik_y y} + \hat{u}^{\infty}_{y-}e^{i\overline{x}-ik_y y}. \end{aligned} \tag{3.6}$$

Using (2.8) and (2.9), the leading-order streamwise and wall-normal velocities in region I are

$$\begin{aligned} \overline{u}_{out} =& 0, \\ \overline{v}_{out} =& -\frac{ie^{i\overline{x}}}{k_z}\left\{\frac{\hat{u}^{\infty}_{y+} + \hat{u}^{\infty}_{y-}}{e^{2\gamma h} - e^{-2\gamma h}}\left[\left(e^{-2\gamma h}-1\right)e^{\gamma y} + \left(1-e^{2\gamma h}\right)e^{-\gamma y}\right] + \hat{u}^{\infty}_{y+}e^{ik_y y}\right. \\ & \left. + \hat{u}^{\infty}_{y-}e^{-ik_y y}\right\}. \end{aligned} \tag{3.7}$$

Similar solutions have been found by Duck (2005) in his analysis of the channel entrance flow, where the boundary-layer perturbation was given by the Luchini mode (Luchini 1996). The leading-order spanwise velocity $\overline{w}_{out}$ can be found from (3.5) for $m = z$ or by using (3.7) and the continuity equation (2.24). It reads

$$\overline{w}_{out} = \frac{i(\hat{u}^{\infty}_{y+} + \hat{u}^{\infty}_{y-})e^{i\overline{x}}}{e^{2\gamma h} - e^{-2\gamma h}}\left[\left(e^{-2\gamma h}-1\right)e^{\gamma y} + \left(e^{2\gamma h}-1\right)e^{-\gamma y}\right] + \hat{u}^{\infty}_{z+}e^{i\overline{x}+ik_y y} + \hat{u}^{\infty}_{z-}e^{i\overline{x}-ik_y y}. \tag{3.8}$$

As the channel walls are approached, $\overline{w}_{out}$ drives the inner flows in the viscous regions II. In region II the spanwise viscous diffusion effects do not play a leading role and thus the flow field is described by the unsteady boundary-layer equations (LWG99). The inner solution for the spanwise velocity is $\overline{w}_{in} = \overline{w}_{com}F'(\eta)$, found by use of (4.13) in LWG99, where the common parts $\overline{w}_{com}$ are

$$\overline{w}_{com}(\overline{x}) = \overline{w}_{out}(y=0,2h) = \frac{\pm i(\hat{u}^{\infty}_{y+} + \hat{u}^{\infty}_{y-})e^{i\overline{x}}}{e^{2\gamma h} - e^{-2\gamma h}}\left(e^{-2\gamma h} + e^{2\gamma h} - 2\right) + e^{i\overline{x}}(\hat{u}^{\infty}_{z+} + \hat{u}^{\infty}_{z-}), \tag{3.9}$$

where the $+$ sign is used for $y=0$ and the $-$ sign is used for $y=2h$.

The composite spanwise velocity in the lower channel half is

$$\overline{w} = \frac{i(\hat{u}^{\infty}_{y+} + \hat{u}^{\infty}_{y-})e^{i\overline{x}}}{e^{2\gamma h} - e^{-2\gamma h}} \left[\left(e^{-2\gamma h} - 1\right) e^{\gamma y} + \left(e^{2\gamma h} - 1\right) e^{-\gamma y}\right] + \hat{u}^{\infty}_{z+} e^{i\overline{x} + ik_y y} + \hat{u}^{\infty}_{z-} e^{i\overline{x} - ik_y y} + \overline{w}_{com}\left(F' - 1\right). \tag{3.10}$$

The solution (3.10) is not needed for the numerical computation in region V because $\overline{w}$ is absent from equations (2.21) and (2.22). However, it is crucial to compute $\overline{w}_{com}$ because it univocally determines the amplitude of the inner streamwise and wall-normal velocities. The streamwise velocity component in region I of the lower channel half is therefore $\overline{u}_{in} = \overline{w}_{com}\overline{x}\eta F''/2$, found using (4.13) in LWG99. As $\overline{u}_{out} = 0$,

$$\overline{u} = \overline{w}_{com}\overline{x}\frac{\eta F''}{2} \tag{3.11}$$

is valid across the whole lower channel half. The asymptotic approach is clearly an invaluable tool as the amplitude of the streamwise perturbation velocity is uniquely linked to the oncoming free-stream flow characteristics through $\overline{w}_{com}$, given in (3.9). In other approaches, based on eigenvalue solutions or optimal perturbations, this essential relation is absent and therefore the streak amplitude must be assigned arbitrarily.

The composite wall-normal velocity $\overline{v}$ is found by first summing the outer solution (3.7) and the inner solution obtained by multiplying the region-II wall-normal velocity (4.13) in LWG99 by the amplitude $\overline{w}_{com}$ and by $(2\overline{x})^{1/2}$ on using (4.1) in LWG99. The common part, i.e., the large-η limit of the region-II solution, is then subtracted. The common part also emerges from the second-order term of the small-y Taylor expansion of the outer solution (3.7), while the leading-order term vanishes because of the no-penetration condition (3.3). The composite wall-normal velocity is therefore

$$\overline{v} = \underbrace{-\frac{ie^{i\overline{x}}}{k_z}\left\{\frac{\hat{u}^{\infty}_{y+} + \hat{u}^{\infty}_{y-}}{e^{2\gamma h} - e^{-2\gamma h}}\left[\left(e^{-2\gamma h} - 1\right) e^{\gamma y} + \left(1 - e^{2\gamma h}\right) e^{-\gamma y}\right] + \hat{u}^{\infty}_{y+} e^{ik_y y} + \hat{u}^{\infty}_{y-} e^{-ik_y y}\right\}}_{\text{outer solution}}$$
$$+ \underbrace{\frac{\overline{w}_{com}}{4}\left(\frac{2\overline{x}}{\mathcal{F}}\right)^{1/2}\left(\eta^2 F'' - 3\eta F' - F\right)}_{\text{inner solution}} + \underbrace{\overline{w}_{com}\left(\frac{2\overline{x}}{\mathcal{F}}\right)^{1/2}\eta}_{\text{common part}}. \tag{3.12}$$

The initial conditions for $\left\{\overline{u}^{(0)}, \overline{v}^{(0)}, \overline{w}^{(0)}\right\}$, defined in (2.9), are also found through a composite solution. The solution for the streamwise velocity $\overline{u}^{(0)}$ is found by combining the outer solution (3.5) for $m = x$ and the inner solution given by (4.13) in LWG99, valid for $\mathcal{F} = \mathcal{O}(1)$ and $\overline{x} \ll 1$. It reads:

$$\overline{u}^{(0)} = e^{i\overline{x}}\left(\hat{u}^{\infty}_{x+} e^{ik_y y} + \hat{u}^{\infty}_{x-} e^{-ik_y y}\right) + \left(\hat{u}^{\infty}_{x+} + \hat{u}^{\infty}_{x-}\right) e^{i\overline{x}}\left[\frac{(\eta F')' + F'}{2} - 1\right]. \tag{3.13}$$

The first term in (3.5) can be neglected because it is $\mathcal{O}(k_x)$. The inner solution for the wall-normal velocity $\overline{v}^{(0)}$ is found by (4.13) in LWG99, which is also valid for $\mathcal{F} = \mathcal{O}(1)$ and $\overline{x} \ll 1$. It reads:

$$\overline{v}^{(0)}_{in} = \frac{\hat{u}^{\infty}_{x+} + \hat{u}^{\infty}_{x-}}{2(2\overline{x}\mathcal{F})^{1/2}}\left[\eta(\eta F')' - F\right]. \tag{3.14}$$

Physically this perturbation velocity represents a wall-normal blowing/suction effect, an

unsteady analogue to the one experienced by the base-flow Blasius boundary layer. In the Blasius case, the base wall-normal velocity is generated by the free-stream uniform U^*_∞, while $\overline{v}^{(0)}_{out}$ is driven by $\overline{u}^{(0)}_{out}$. As $\overline{u}^{(0)}_{out}(y=0,2h)=\hat{u}^\infty_{x+}+\hat{u}^\infty_{x-}$, the physical transpiration wall-normal velocities from the two boundary layers attached to the channel walls are opposite and equal in magnitude at each time and z. They induce the inviscid velocity field $\mathbf{u}^{(1)}_1$ in (3.1) and the associated wall-normal pressure gradient that, differently from $\overline{v}$ which may be finite at the centreline, takes $\overline{v}^{(0)}_{out}$ to zero at $y=h$. The velocity potential ϕ_1 satisfies

$$\nabla^2\phi_1=0, \tag{3.15}$$

subject to

$$\frac{\partial\phi_1}{\partial y}=\lim_{\eta\to\infty}\overline{v}^{(0)}_{in}=\beta\frac{\hat{u}^\infty_{x+}+\hat{u}^\infty_{x-}}{2(2\overline{x}\mathcal{F})^{1/2}}e^{ikz-ikxt} \quad \text{at} \quad y=0, \quad x>0, \tag{3.16a}$$

$$\frac{\partial\phi_1}{\partial y}=-\beta\frac{\hat{u}^\infty_{x+}+\hat{u}^\infty_{x-}}{2(2\overline{x}\mathcal{F})^{1/2}}e^{ikz-ikxt} \quad \text{at} \quad y=2h, \quad x>0. \tag{3.16b}$$

Similar to the problem of solving (3.2), (3.15) cannot be solved in the infinite strip $-\infty<x<\infty$, $0\leqslant y\leqslant 2h$ because the boundary conditions at $y=0,2h$ for $x<0$ are unknown. In our region of interest, $x\gg1$, the second derivative of ϕ_1 with respect to x is asymptotically smaller than the other derivatives as long as $k_x\ll\overline{x}\ll1$ because of the $(2\overline{x})^{-1/2}$ behaviour of the boundary conditions (3.16a) and (3.16b). It follows that, by separating the variables and expressing $\phi_1=\hat{\phi}_1(y)\exp(ik_zz-ik_xt)/(2\overline{x})^{1/2}$, we find

$$\hat{\phi}_1=\beta\frac{\hat{u}^\infty_{x+}+\hat{u}^\infty_{x-}}{2k_z\mathcal{F}^{1/2}}\left[\frac{e^{k_z(y-h)}+e^{-k_z(y-h)}}{e^{-k_zh}-e^{k_zh}}\right]. \tag{3.17}$$

The composite $\overline{v}^{(0)}$ in the lower channel half reads

$$\overline{v}^{(0)}=\frac{\hat{u}^\infty_{x+}+\hat{u}^\infty_{x-}}{2(2\overline{x}\mathcal{F})^{1/2}}\left\{\eta(\eta F')'-F+\beta\left[\frac{e^{k_z(y-h)}-e^{-k_z(y-h)}}{e^{-k_zh}-e^{k_zh}}-1\right]\right\}. \tag{3.18}$$

The symmetry is again used to construct the solution in the upper channel half. It is easily verified that $k_x\overline{v}^{(0)}$ is asymptotically smaller than $ik_z\overline{v}$ and $\overline{u}^{(0)}$ in the region of interest $k_x/R_\lambda\ll\overline{x}\ll1$, as required by expansion (2.9).

Differently from the leading-order components where $\overline{w}_{out}$ is needed to determined the amplitude of $\{\overline{u}_{in},\overline{v}_{in}\}$, it is not necessary to compute $\overline{w}^{(0)}$ as we have already found $\{\overline{u}^{(0)},\overline{v}^{(0)}\}$ to start the integration of the boundary-region equations (2.21) and (2.21). The component $\overline{w}^{(0)}$ induces a boundary-layer perturbation of the same order as the streamwise slip velocity, and it would be needed if an initial condition of second-order accuracy were constructed. The spanwise velocity $\overline{w}^{(0)}$ can be computed by the composite solution, where the outer solution is obtained by using (3.17) and by solving (A3) and (A4) in Ricco (2009) when $\mathcal{F}=\mathcal{O}(1)$ (it is null when $\mathcal{F}\gg1$). The pressure disturbance in (A3) in Ricco (2009) is found by again using (3.17) and equation (3.2) in LWG99. We note that analytical expression for $\{\overline{u}^{(0)}_{in},\overline{v}^{(0)}_{in}\}$ are instead valid for $\mathcal{F}=\mathcal{O}(1)$.

Figure 3 shows velocity profiles for a streamwise case, i.e., $\hat{u}^\infty_{x+}=\hat{u}^\infty_{x-}$. The streamwise velocity profiles $\Re(\overline{u})$ and $\Re(\overline{u}^{(0)})$ are symmetric with respect to the centerline (top left graph), while $\Re(\overline{v})$ is antisymmetric (top right graph) because $\hat{u}^\infty_{y+}$ and $\hat{u}^\infty_{y-}$ have opposite signs due to the continuity relation (2.2). The wall-normal velocity $\Re(\overline{v}^{(0)})$ is antisymmetric because it is generated by the opposite boundary-layer transpiration

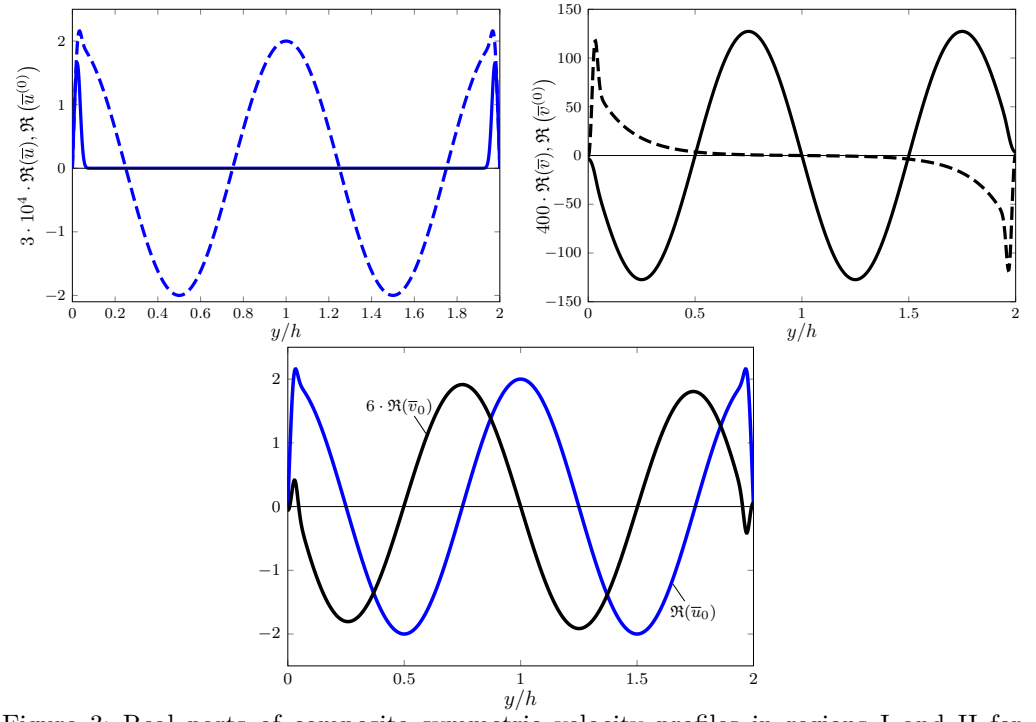

Figure 3: Real parts of composite symmetric velocity profiles in regions I and II for $\overline{x} = 10^{-4}$, $R_\lambda = 1000$, $k_x = 0.001$, $k_y = 2\pi$, $\hat{u}^\infty_{x+} = \hat{u}^\infty_{x-} = \hat{u}^\infty_{z+} = \hat{u}^\infty_{z-} = 1$, $\hat{u}^\infty_{y+} = -2 = -\hat{u}^\infty_{y-}$, and $h = 1$. Top left: Real parts of $\overline{u}$ (solid line) and $\overline{u}^{(0)}$ (dashed line). Top right: Real parts of $\overline{v}$ (solid line) and $\overline{v}^{(0)}$ (dashed line). Bottom: Real parts of the velocity components $\overline{u}_0$ and $\overline{v}_0$.

velocities given in (3.16*a*) and (3.16*b*). The bottom graph of figure 3 shows that the combined $\Re(\overline{u}_0)$ is symmetric and the combined $\Re(\overline{v}_0)$ is antisymmetric.

The composite solutions (3.11), (3.12), (3.13), and (3.18) for $\overline{u}, \overline{v}, \overline{u}^{(0)}$, and $\overline{v}^{(0)}$ in regions I and II are used as initial conditions for the computation in regions V and VI.

3.2. *Perturbation flow in regions III and IV*

The outer expressions (3.7) do not take into account the viscous decay as they are valid in the very proximity of $\overline{x} = 0$. As the outer flow develops downstream through region IV, viscous effects become important. The flow in regions III and IV can be found by a composite solution. The expression for the outer velocity field in region IV is derived analytically by writing

$$\mathbf{u} = \left\{ \frac{\partial \psi}{\partial y}, -\frac{\partial \psi}{\partial x}, 0 \right\} + \varepsilon \mathbf{u}_{out} e^{i(k_z z - k_x t)} + \text{c.c.}, \tag{3.19}$$

where the streamfunction $\psi(\overline{x}, y)$ is given in the Supplementary Material (S1.6) and (S1.11). The outer velocity $\mathbf{u}_{out}$ satisfies the parabolic region-IV momentum equations (5.9) on page 181 in LWG99, but in our case the initial conditions are given by our solution in region I, i.e., (3.7) for $\overline{u}_{out}$ and $\overline{v}_{out}$, and (3.8) for $\overline{w}_{out}$. The solution is found

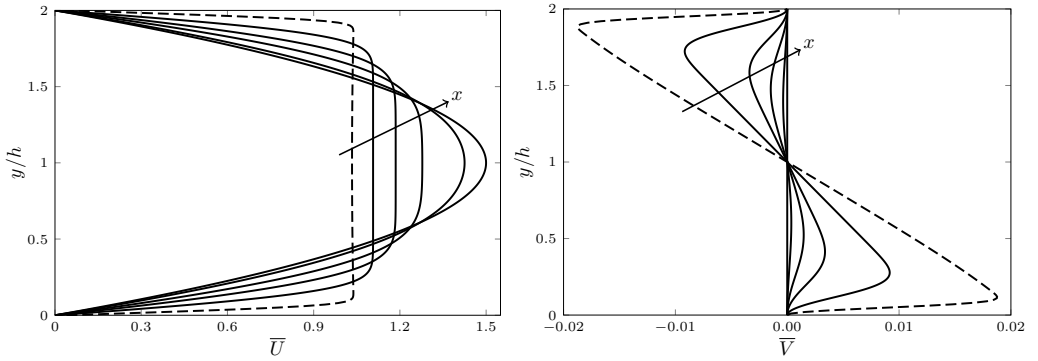

Figure 4: Streamwise (left) and wall-normal (right) base-flow velocity profiles. The solid lines denote the solutions at $x/(h^2R_\lambda) = 0.003, 0.012, 0.03, 0.08, 0.4$ obtained by numerically solving the boundary-layer equations (2.11)-(2.10). The dashed lines show the composite solution of the streamwise velocity (S1.15) (left) and of the wall-normal velocity (S1.16) (right) at $x/(h^2R_\lambda) = 0.0004$.

by separation of variables,

$$\begin{aligned}
\overline{u}_{out} =& 0, \\
\overline{v}_{out} =& -\frac{i}{k_z}\left\{\frac{\left(\hat{u}^\infty_{y+}+\hat{u}^\infty_{y-}\right)e^{i\overline{x}}}{e^{2\gamma h}-e^{-2\gamma h}}\left[\left(e^{-2\gamma h}-1\right)e^{\gamma\psi}+\left(1-e^{2\gamma h}\right)e^{-\gamma\psi}\right]\right. \\
&\left.+e^{i\overline{x}-\left(k_y^2+k_z^2\right)\overline{x}/\mathcal{F}}\left(\hat{u}^\infty_{y+}e^{ik_y\psi}+\hat{u}^\infty_{y-}e^{-ik_y\psi}\right)\right\}, \qquad (3.20) \\
\overline{w}_{out} =& \frac{i(\hat{u}^\infty_{y+}+\hat{u}^\infty_{y-})e^{i\overline{x}}}{e^{2\gamma h}-e^{-2\gamma h}}\left[\left(e^{-2\gamma h}-1\right)e^{\gamma\psi}+\left(e^{2\gamma h}-1\right)e^{-\gamma\psi}\right]+ \\
&e^{i\overline{x}-\left(k_y^2+k_z^2\right)\overline{x}/\mathcal{F}}\left(\hat{u}^\infty_{z+}e^{ik_y\psi}+\hat{u}^\infty_{z-}e^{-ik_y\psi}\right).
\end{aligned}$$

As depicted in figure 1, the base-flow pressure gradient only has a second-order effect through the $\overline{x}$-dependency of $\psi(\overline{x}, y)$. The inner solution is found numerically by solving the boundary-region equations (5.2)-(5.5) on page 180 of LWG99, complemented by mixed-type boundary conditions obtained by asymptotically matching the solution of the large-η equations (5.16)-(5.19) on page 181 of LWG99 with the outer solution (3.20). This numerical calculation is however not pursued herein because our region-V solution includes the solutions of regions III and IV and covers the whole streamwise flow evolution as the base-flow pressure gradient is accounted for at leading order.

4. Flow development in regions V and VI

In §3 the base and perturbation flows are influenced by the confinement of the channel, but the streamwise location is sufficiently upstream for the base-flow streamwise pressure gradient not to play a leading-order role. In the present section, we consider regions V and VI, i.e., downstream locations where the base-flow pressure gradient instead plays a leading order role on the base flow and therefore on the perturbation flow. In region VI, the pressure gradient adjusts downstream to a constant value as the base flow develops to the fully-developed Poiseuille flow. The base-flow profiles are obtained by solving (2.11)-(2.13) and the perturbation profiles are found by solving (2.21) and (2.22).

The base-flow streamwise and wall-normal velocity profiles across the channel are shown in figure 4 for various streamwise positions. The base-flow streamwise velocity

Fluid	U^*_∞ [m s^{-1}]	ν^* [m^{2}s^{-1}] $\times 10^6$	R^*_∞ [m^{-1}] $\times 10^{-3}$	h^* [m] $\times 10^3$	λ^*_z, λ^*_y [m] $\times 10^3$	λ^*_x [m]	R_λ	k_x	k_y	R_h	λ_{xh}	λ_{yh}	λ_{zh}
Water	0.1	1	100	15	15	0.8	1500	0.118	2π	1500	53.3	1	1
Air	1.3	13	100	15	15	0.8	1500	0.118	2π	1500	53.3	1	1

Table 1: Flow parameters for water and air channel experiments. The unit Reynolds number is $R^*_\infty = U^*_\infty/\nu^*$.

evolves to the parabolic Poiseuille profile, while the wall-normal velocity decreases to zero. The development of the base flow is studied in more detail in the Supplementary Material §S2.

The scaling adopted in §2, which leads to $\overline{\mathbf{u}}_\mathbf{0} = \overline{\mathbf{u}}_\mathbf{0}(\overline{x}, y; R_\lambda, k_x, k_y, h, \hat{u}^\infty_{x\pm}, \hat{u}^\infty_{z\pm})$, is useful for the asymptotic analysis and it relates directly to the open-boundary-layer case of LWG99. However, it is does not convey an immediate physical meaning as, for example, the scaled frequency k_x appears as an independent variable and in the scaling of $\overline{x}$. We therefore express the solution as $\overline{\mathbf{u}}_\mathbf{0} = \overline{\mathbf{u}}_\mathbf{0}(x_h, y_h; R_h, \lambda_{xh}, \lambda_{yh}, \lambda_{zh}, \hat{u}^\infty_{x\pm}, \hat{u}^\infty_{z\pm})$, where the subscript h indicates scaling by the half channel height h^*, i.e., $\lambda_{jh} = \lambda^*_j/h^*$, where $j = x, y, z$, $x_h = x^*/h^*$, and $y_h = y^*/h^*$.

We first study the velocity and pressure profiles of a reference case that is representative of realistic low-speed water and air channel experiments. Table 1 presents the flow parameters of these cases. We then study the effect of the inflow parameters on the perturbation field.

4.1. *Initial reference perturbation flow*

The appropriate specification of the composite initial condition requires a smooth matching with the numerical solutions of the boundary-region equations (2.21) and (2.22) at small x_h locations. This matching is monitored by comparison in figure 5. Figure 5 shows that the asymptotic profiles (dashed lines), used as initial conditions for the numerical integration of the boundary-region equations, are consistent with the numerical solutions (solid lines) at small x_h. The streamwise $\overline{u}$ profiles resemble the profiles of the Klebanoff modes appearing in free-stream open boundary layers (shown in figure 3 on page 184 of LWG99), although the peak of the numerical profiles is slightly closer to the channel centerline. The confinement of the channel has an influence on the amplitude and growth rate of $\overline{u}$ through $\overline{w}_{com}$, given in (3.9), because $\overline{w}_{com}$ depends on h.

We further note that at these locations the dominant part of the total streamwise disturbance velocity $\overline{u}_0$ is due to $\overline{u}^{(0)}$, which is given in (3.13) and is caused by the direct free-stream forcing action of the inviscid streamwise velocity in (3.5). The part due to $\overline{u}$ is smaller, which means that the streaks have not formed yet and do not dominate the boundary layers over the channel walls.

4.2. *Reference perturbation flow in regions V and VI*

The downstream evolution of the disturbance field for the conditions of Table 1 is investigated for the cases of perturbations at the channel entrance that are symmetric ($\hat{u}^\infty_{x,z,\pm} = 1.0$) and anti-symmetric ($\hat{u}^\infty_{x,z,+} = 1.0$, $\hat{u}^\infty_{x,z,-} = -1.0$) with respect to the channel centreline. The inflow perturbations are streamwise-stretched vortices that are round in cross-sectional $y - z$ planes because the spanwise and the wall-normal wavelengths are equal and much shorter than the streamwise wavelength. As discussed

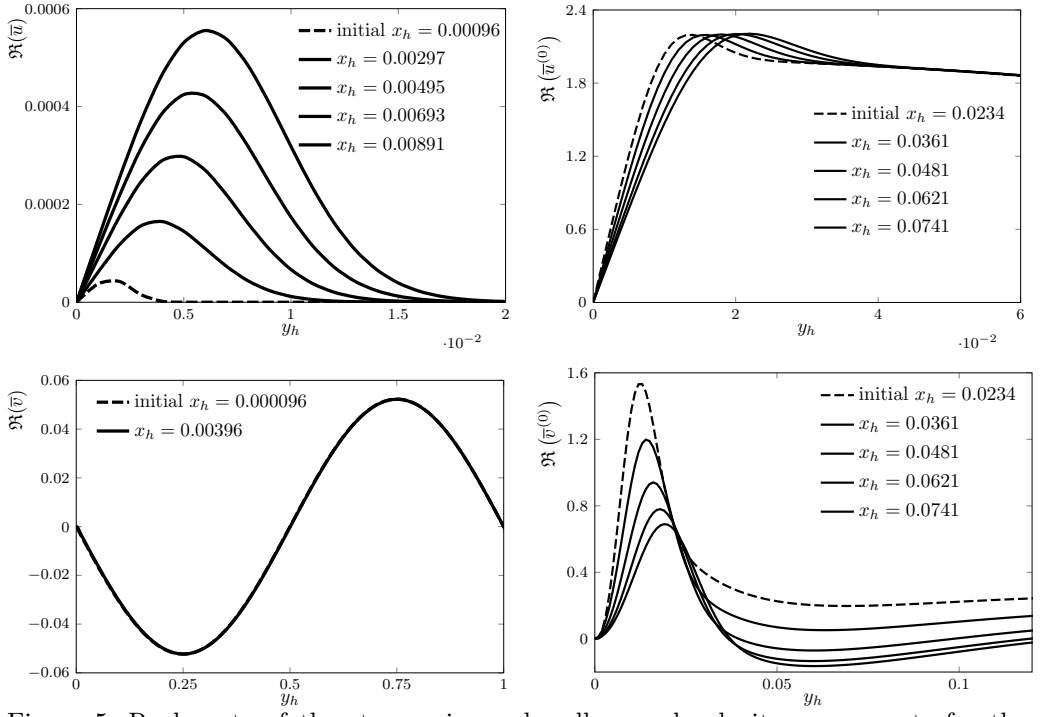

Figure 5: Real parts of the streamwise and wall-normal velocity components for the reference conditions of Table 1 generated by an oncoming symmetric gust disturbances, i.e., $\hat{u}^{\infty}_{x,y,\pm} = 1.0, \hat{u}^{\infty}_{z,\pm} = 1.0$. The solid lines indicate the numerical solutions of the boundary-region equations (2.21) and (2.22) and the dashed lines indicate the asymptotic composite solutions used as initial conditions of the numerical calculations: (3.11) for $\overline{u}$, (3.13) for $\overline{u}^{(0)}$, (3.12) for $\overline{v}$, and (3.18) for $\overline{v}^{(0)}$.

in §2.3, at this bulk Reynolds number, $R_h = 1500$, no TS-waves exist, but nevertheless an intense transient growth is detected. This growth is monitored by the energy of the perturbation, defined as

$$\mathcal{E}(x_h) = \underbrace{\frac{1}{2}\int_0^2 |\overline{u}_0|^2 \mathrm{d}y_h}_{\mathcal{E}_u} + \underbrace{\frac{1}{2}\int_0^2 |\overline{v}_0|^2 \mathrm{d}y_h}_{\mathcal{E}_v} + \underbrace{\frac{1}{2}\int_0^2 |\overline{w}_0|^2 \mathrm{d}y_h}_{\mathcal{E}_w}, \tag{4.1}$$

where the velocity components $\overline{u}_0, \overline{v}_0, \overline{w}_0$ are defined in (2.9). Figure 6 (left) shows that, while at the entrance the three velocity components have the same intensity, the streamwise velocity component generated by a symmetric gust disturbance is the major contributor to the perturbation dynamics as the total energy grows from the channel inlet, while the other two velocity components decay at the same rate. Downstream of $x_h = 20$, the total energy is almost entirely due to $\overline{u}_0$ and it decreases due to viscous effects. The entrance region, estimated through the centerline base-flow velocity, terminates at $x_h = 258$ and therefore the transient growth is wholly confined in region V, upstream of the fully developed region VI.

Figure 6 (right) reveals that most of the perturbation energy is confined within the boundary layers as the wall-normal location $y_{\mathcal{E}}$ of the maximum energy $\mathcal{E}$ is smaller than the boundary layer thickness δ_h, depicted in figure S5 (left). The inset of figure 6 (right)

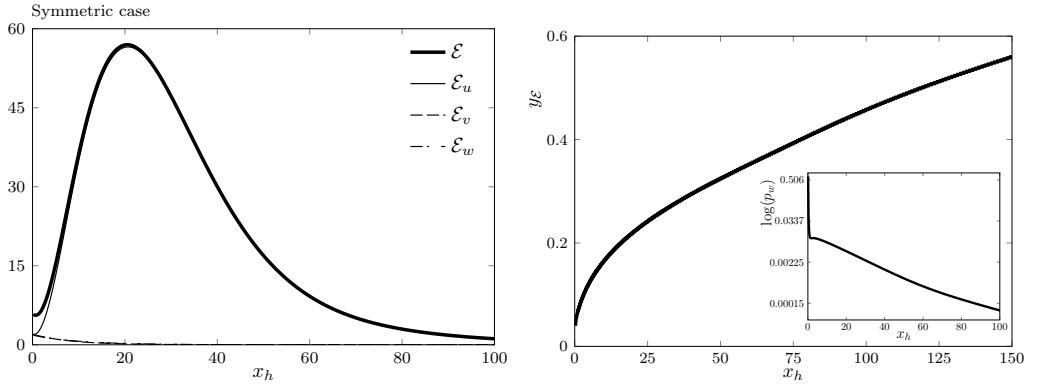

Figure 6: Left: streamwise evolution of the perturbation energy $\mathcal{E}$ and of its three parts $\mathcal{E}_u, \mathcal{E}_v, \mathcal{E}_w$ related to the velocity components. Right: streamwise evolution of the wall-normal location of the maximum $\mathcal{E}$ and of the amplitude of the wall perturbation pressure p_w (inset). All trends are for the case of a symmetric gust disturbance.

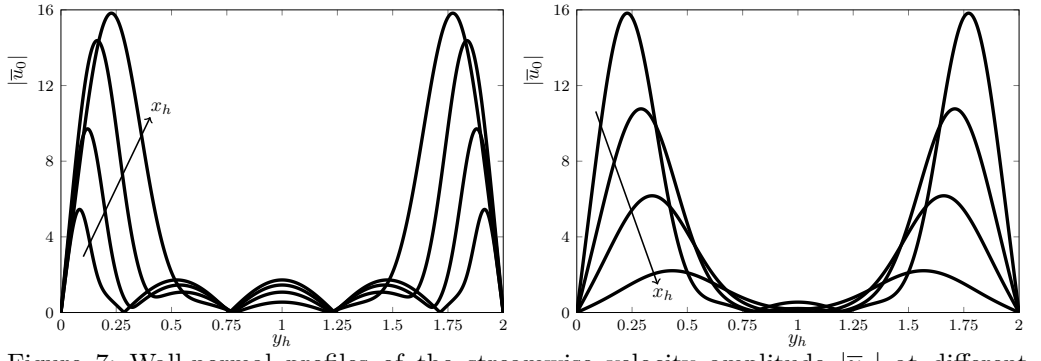

Figure 7: Wall-normal profiles of the streamwise velocity amplitude $|\overline{u}_0|$ at different streamwise locations for the case of a symmetric gust disturbance. Left: growing disturbances at $x_h = 2, 4.7, 9.8, 21.7$. Right: decaying disturbances at $x_h = 21.7, 38.7, 55.6, 89.6$.

displays the downstream evolution of the magnitude of the pressure at the wall, i.e.,

$$p_w(x_h) = |\overline{p}_0(y_h = 0)| = k_{zh}^{-2} \left| \frac{\partial^2 \overline{w}_0}{\partial y_h^2} \right|_{y_h=0}, \tag{4.2}$$

where the relation to the spanwise velocity is found from (2.25). It decays monotonically, sharply up to $x_h = 2$ and more mildly further downstream.

The wall-normal profiles of $|\overline{u}_0|$ are shown in figure 7 (left for growing disturbances and right for decaying disturbances). The disturbance near the centerline always decays because of the almost total absence of base-flow velocity gradients that instead enhance the intensity of the perturbation near the walls. The maximum of $|\overline{u}_0|$ moves towards the centerline at all streamwise locations. The spanwise velocity $|\overline{w}_0|$ in figure 8 (left) decays almost at the same rate irrespectively of the wall-normal location and so does the wall-normal velocity $|\overline{v}_0|$ (not shown). Figure 8 (right) confirms that the pressure $|\overline{p}_0|$ is related to $|\overline{w}_0|$ as they share the same locations of the maxima, although the overall maximum pressure disturbance is found at the wall.

The flow dynamics triggered by the anti-symmetric gust disturbance imposed at the channel entrance presents notable differences from the one of the symmetric disturbance.

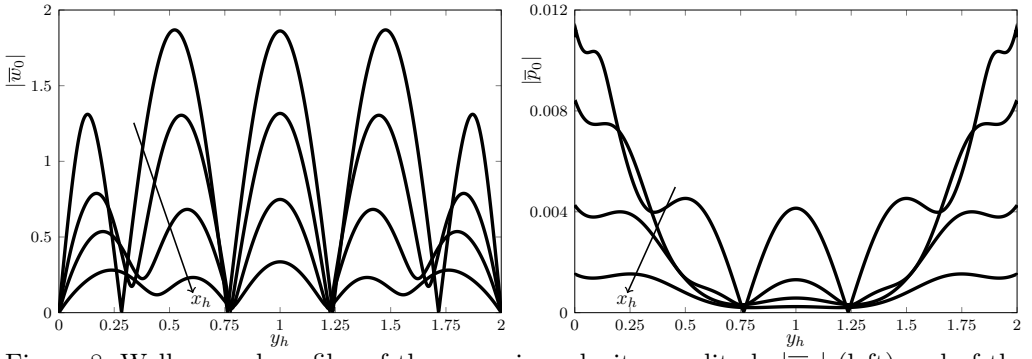

Figure 8: Wall-normal profiles of the spanwise velocity amplitude $|\overline{w}_0|$ (left) and of the pressure amplitude $|\overline{p}_0|$ (right) at $x_h = 2, 9.8, 21.7, 38.7$ generated by a symmetric gust disturbance.

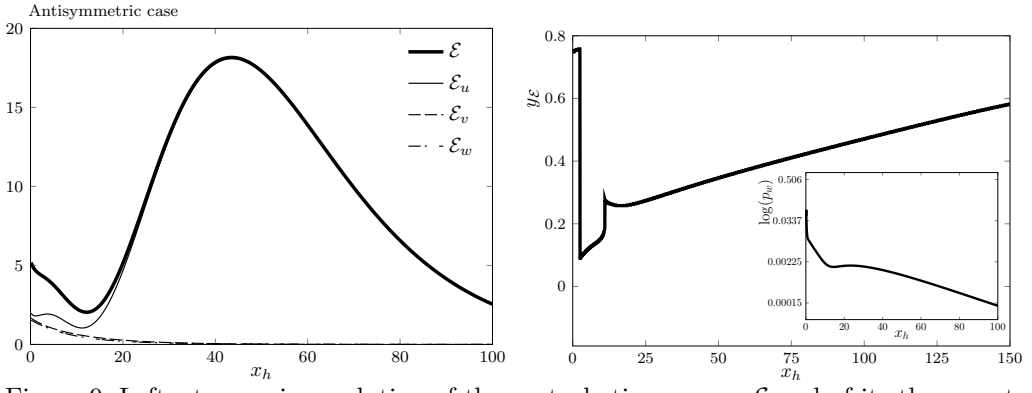

Figure 9: Left: streamwise evolution of the perturbation energy $\mathcal{E}$ and of its three parts $\mathcal{E}_u, \mathcal{E}_v, \mathcal{E}_w$ related to the velocity components. Right: streamwise evolution of the wall-normal location of the maximum $\mathcal{E}$ and of the amplitude of the wall perturbation pressure p_w (inset). All trends are for the antisymmetric-gust case.

Figure 9 (left) shows that, while the total energy is still primarily due to $|\overline{u}_0|$, the streamwise velocity oscillates mildly up to $x_h = 5$, decays up to $x_h = 12$, and then grows to a maximum that is only about a third of the one attained by the flow forced by the symmetric-gust disturbance. This maximum also occurs at double the distance of the symmetric-gust flow. The cross-flow velocity components decay as in the symmetric-gust case. In the right graph of figure 9, the maximum energy location $y_\mathcal{E}$ is confined within the boundary layers, except in the proximity of the channel entrance. The trend is not continuous because different local maxima emerge as the global maximum during the downstream flow evolution.

The streamwise oscillatory behaviour near the channel inlet occurs within the boundary layers, while the perturbation in the channel core decreases monotonically, as shown in figure 10 (left). During the growth and subsequent decay (figure 10, right), the wall-normal $|\overline{u}_0|$ profiles resemble the decaying perturbations in figure 7 (right).

4.3. *Effect of Reynolds number*

The change of the downstream evolution of the total energy $\mathcal{E}$ as the bulk Reynolds number R_h varies is shown figure 11 for the symmetric-gust case (left) and the anti-symmetric-gust case (right). As R_h increases, the energy generated by the symmetric

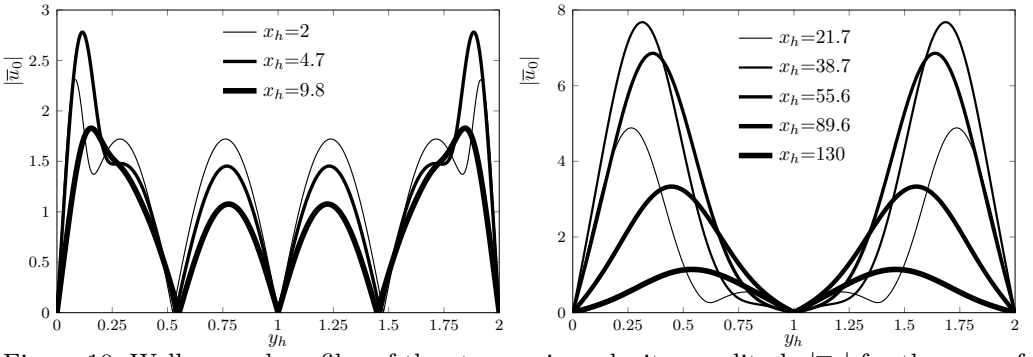

Figure 10: Wall-normal profiles of the streamwise velocity amplitude $|\overline{u}_0|$ for the case of the antisymmetric-gust disturbance at different streamwise locations.

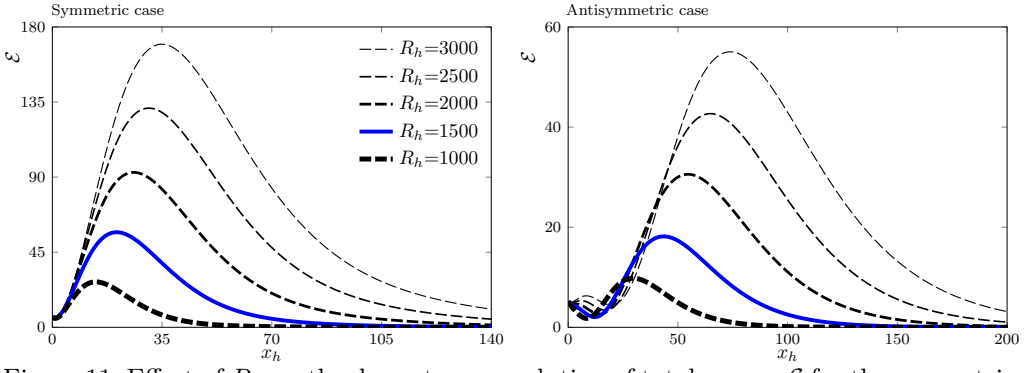

Figure 11: Effect of R_h on the downstream evolution of total energy $\mathcal{E}$ for the symmetric-gust case (left) and the anti-symmetric gust case (right). The blue solid line in this figure and in figures 13, 15, and 14 indicates the reference case of Table 1.

gust at the channel entrance is initially largely unaffected up to about $x_h = 5$, while the energy of the anti-symmetric disturbance decays up to about $x_h = 15$ for $R_h \leqslant 2000$ and oscillates spatially up to about $x_h = 20$ for $2500 < R_h < 3000$. This initial oscillatory behaviour is due to the streamwise velocity component as the cross-flow velocities decay monotonically. It is a peculiar feature of the response of the channel-entry shear layers to oncoming vortical disturbances because it does not occur in unconfined boundary layers exposed to free-stream disturbances (LWG99). Further downstream the disturbance energy increases monotonically with R_h and the maximum occurs at larger streamwise locations as R_h increases. This dependence on the Reynolds number also occurs in open boundary layers exposed to free-stream vortical structures and the scaled spanwise wavenumber $\kappa = k_z/(k_x R_\lambda)^{1/2}$ is the governing parameter, as shown by LWG99. In LWG99's figures 5 and 6, as κ decreases from 1 to 0.1 the streamwise velocity, which dominates the total energy, increases and its maximum occurs further downstream. This result is consistent with the cases of figure 11, for which κ decreases in the range $0.33 < \kappa < 0.58$ as R_h increases. The wall-normal locations of the energy maxima move closer to the walls at larger R_h as the boundary layers becomes thinner (not shown).

Some qualitative confirmation of the enhancement of the perturbation intensity as the Reynolds number increases is given by the traces of hot-wire measurements reported by Patel & Head (1969) and shown in figure 12. The air flow was measured at a distance of

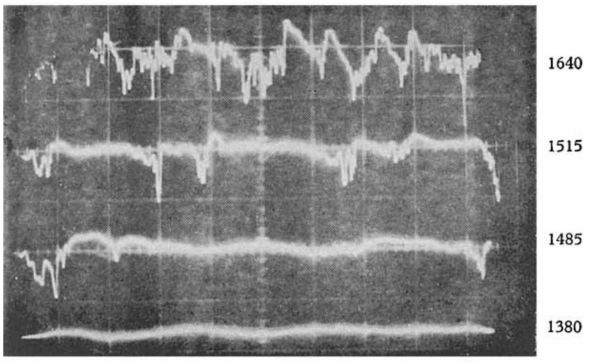

Figure 12: Subcritical enhancement of air-flow perturbations caused by vortical disturbances at the entrance of a channel (Patel & Head 1969). The number on the right is the Reynolds number $2Re_h$.

203 channel heights from the entrance ($x/h = 406$), at which the flow reached its fully-developed parabolic profile for the Reynolds numbers $2Re_h$ given on the right of the images. The perturbations at that downstream location were generated by fluctuations at the entrance of the channel. The air flow was sufficiently disturbed at the channel entrance to become more unstable further downstream as the Reynolds number increased, as predicted by the theoretical results shown in figure 11, despite being linearly stable according to classical stability theory. As Patel & Head (1969)'s measurements were conducted in the fully-developed region, experimental data and nonlinear numerical data in the channel entrance region are needed for a more meaningful comparison.

4.4. *Effect of streamwise wavelength*

The change of the streamwise wavelength λ_{xh} of the oncoming disturbance is inversely proportional to the frequency as the two quantities are related through the free-stream velocity U_∞^* for small-amplitude free-stream convective gusts. As evident in figure 13, the initial energy amplitude is independent of λ_{xh} as this parameter does not appear in the velocity components in (2.3)-(2.4). At streamwise distances up to $x_h = 10$ for both cases, λ_{xh} has no influence on the disturbance growth as all the profiles collapse on one another. Further downstream, oncoming disturbances with longer wavelengths (smaller frequencies) grow more energetically and their maxima occur at larger streamwise locations. The trends at the two highest λ_{xh} overlap (solid red line and dashed white line), showing the independence of the dynamics from the frequency.

Luchini (2000) also predicted the optimal perturbations to be steady, although in that case free-stream vortical disturbances were absent and the perturbations were solely confined within the boundary layer (Andersson *et al.* (1999) assumed the perturbations to be steady). However, the results of the most detrimental perturbation being steady can be misleading because our results in figure 13 show that oncoming perturbations with measurable unsteadiness, i.e., with frequency $f^* = 2\text{Hz}$ ($\lambda_{xh} = 100$) for the air channel in Table 1, may be equally likely to lead to the flow breakdown as they achieve a growth which is very close to the optimal one.

The asymptotic scaling at large λ_{xh} can be studied by use of $\epsilon = k_{xh}R_h \ll 1$, where $k_{xh} = 2\pi/\lambda_{xh}$. The base-flow equations (2.11)-(2.10) rescale as

$$U\frac{\partial U}{\partial \widehat{x}} + \widehat{V}\frac{\partial U}{\partial y} = -\frac{\mathrm{d}P}{\mathrm{d}\widehat{x}} + \widehat{\gamma}\frac{\partial^2 U}{\partial y^2}, \tag{4.3}$$

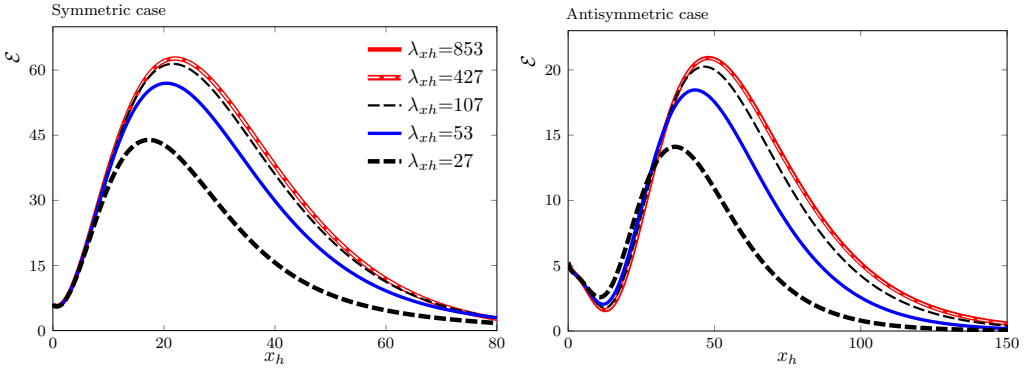

Figure 13: Effect of λ_{xh} on the downstream evolution of total energy $\mathcal{E}$ for the symmetric-gust case (left) and the anti-symmetric-gust case (right).

$$\frac{\partial P}{\partial y} = 0, \quad \frac{\partial U}{\partial \widehat{x}} + \frac{\partial \widehat{V}}{\partial y} = 0, \tag{4.4}$$

where $\widehat{V} = \epsilon V$, $\widehat{x} = x_h/R_h$ and $\widehat{\gamma} = (k_{zh}/2\pi)^2 = \mathcal{O}(1)$. In the limit $\epsilon \to 0$, the boundary-region equations (2.21)-(2.22) reduce to

$$\left(-k_z^2 k_{zh}^2 - k_z^2 \frac{\partial \widehat{V}}{\partial y} + \frac{\partial^3 \widehat{V}}{\partial y^3}\right)\overline{v} - \left(k_z^2 \widehat{V} - \frac{\partial^2 \widehat{V}}{\partial y^2}\right)\frac{\partial \overline{v}}{\partial y} + \left(2k_{zh}^2 + \frac{\partial \widehat{V}}{\partial y}\right)\frac{\partial^2 \overline{v}}{\partial y^2} +$$
$$\widehat{V}\frac{\partial^3 \overline{v}}{\partial y^3} + U\frac{\partial^3 \overline{v}}{\partial \widehat{x}\partial y^2} - \widehat{\gamma}\frac{\partial^4 \overline{v}}{\partial y^4} - \left(k_z^2 U + \frac{\partial^2 U}{\partial y^2}\right)\frac{\partial \overline{v}}{\partial \widehat{x}} - \left(k_z^2 \frac{\partial \widehat{V}}{\partial \widehat{x}} - \frac{\partial^3 \widehat{V}}{\partial \widehat{x}\partial y^2}\right)\widehat{u} - \tag{4.5}$$
$$2\frac{\partial^2 U}{\partial \widehat{x}\partial y}\frac{\partial \widehat{u}}{\partial \widehat{x}} - 2\frac{\partial U}{\partial \widehat{x}}\frac{\partial^2 \widehat{u}}{\partial \widehat{x}\partial y} - \frac{\partial \widehat{V}}{\partial \overline{x}}\frac{\partial^2 \widehat{u}}{\partial y^2} = 0,$$

$$\left(k_{zh}^2 + \frac{\partial U}{\partial \widehat{x}}\right)\widehat{u} + U\frac{\partial \widehat{u}}{\partial \widehat{x}} + \widehat{V}\frac{\partial \widehat{u}}{\partial y} - \widehat{\gamma}\frac{\partial^2 \widehat{u}}{\partial y^2} + \frac{\partial U}{\partial y}\overline{v} = 0, \tag{4.6}$$

where $k_{zh} = 2\pi h^*/\lambda_z^*$ and $\widehat{u} = \overline{u}/\epsilon$. All the terms in (2.21)-(2.22) that are proportional to i, which arise due to the unsteadiness of the oncoming disturbance (2.1), do not appear in (4.5)-(4.6) because the low-frequency disturbance dynamics is now steady at leading order. The analogous scaling for open free-stream boundary layers was first found by LWG99 on page 183-185. In figure 13, the behaviour is consistent with the asymptotic analysis for $\epsilon \ll 1$: R_h is constant for those cases and thus it does not impact on the streamwise scaling $\widehat{x}$, and at leading order the total energy is

$$\mathcal{E} \sim \frac{1}{2}\int_0^2 \left|\frac{k_z}{k_x}\widehat{u}\right|^2 \mathrm{d}y_h = \frac{k_{zh}^2 R_h^2}{2}\int_0^2 |\widehat{u}|^2 \mathrm{d}y_h, \tag{4.7}$$

which is independent of λ_{xh}.

4.5. *Effect of wall-normal wavelength*

Figure 14 shows that the transient growth decreases as the wall-normal wavelength of the oncoming disturbance becomes smaller. This result is due to the more intense viscous dissipation caused by the high velocity gradients at small wavelengths. Therefore the most energetic growth occurs for the largest wavelength, i.e., when λ_y^* spans the whole channel height ($\lambda_{yh} = 2$). For our choice of specified disturbances in (2.3), i.e., with fixed $\hat{u}_{x,z,\pm}^{\infty}$ and wavelengths, the initial amplitude of u_y increases proportionally to λ_{yh} to

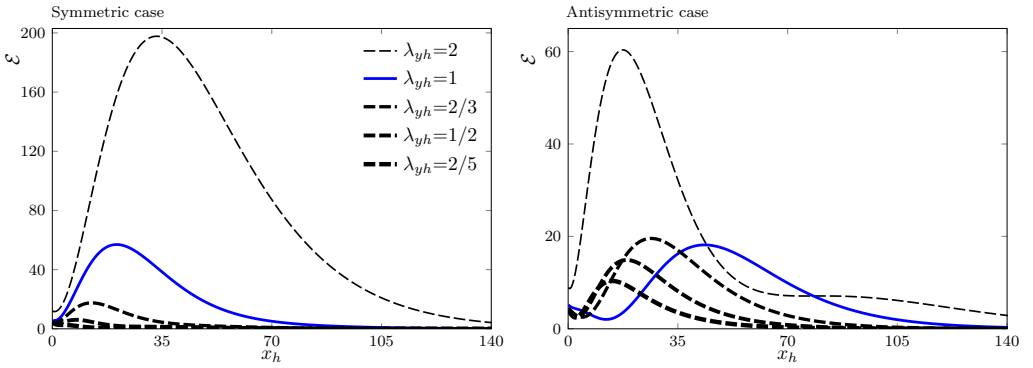

Figure 14: Effect of λ_{yh} on the downstream evolution of total energy $\mathcal{E}$ for the symmetric-gust case (left) and the anti-symmetric-gust case (right).

maintain the solenoidal condition (2.2) at the channel entrance. However, this change of u_y is not the reason for the intense growth at larger λ_{yh} because the disturbance amplifies more than the linear increase proportional to u_y. For wavelengths λ_y^* that are one fifth ($\lambda_{yh} = 2/5$) or shorter than the channel height, no downstream growth of the symmetric disturbance is detected because of viscous effects, while the attenuation is less effective on the anti-symmetric disturbance. The location of the maximum energy is found to be closer to the channel entrance as λ_{yh} drops.

An important observation is that the effect of λ_{yh} on the disturbance evolution cannot be investigated through the non-normality of the eigenfunctions of the developing boundary layers on the channel walls. This limitation occurs because an eigenvalue-based approach would model the near-entrance disturbance as wholly confined within the near-wall boundary layers, whereas λ_{yh} is a parameter that solely pertains to the oncoming external flow and does not enter the classical stability problem of the boundary layer. The spanwise and the streamwise wavelengths can instead enter the eigenvalue problem directly because the base flow is spanwise independent and steady. The boundary-region approach based on (2.21)-(2.22) can account for the characteristics of the oncoming flow because it is an initial-value problem where the specification of the oncoming disturbances at the channel entry is crucial for the flow dynamics downstream.

4.6. *Effect of spanwise wavelength*

The influence of the variation of the spanwise wavelength λ_{zh} is shown in figure 15. There exists an optimal λ_{zh} (the reference $\lambda_{zh} = 1$ for the symmetric disturbance and $\lambda_{zh} = 2$ for the antisymmetric disturbance) that leads to the most energetic growth. Disturbances with very small λ_{zh} are strongly influenced by viscous dissipation that hampers their growth. Oncoming disturbances with large spanwise wavelength, $\lambda_{zh} = 4, 8$ are almost two-dimensional and, although they do not produce the maximum growth, they persist further downstream because they are less affected by viscous dissipation due to spanwise shear effects. The perturbations with the largest tested wavelength, $\lambda_{zh} = 16$, decay monotonically, confirming that the transient streaky growth is a three-dimensional phenomenon.

5. Conclusions

In this paper we have presented a theoretical and numerical analysis of the entrainment and growth of unsteady three-dimensional vortical disturbances in the entrance

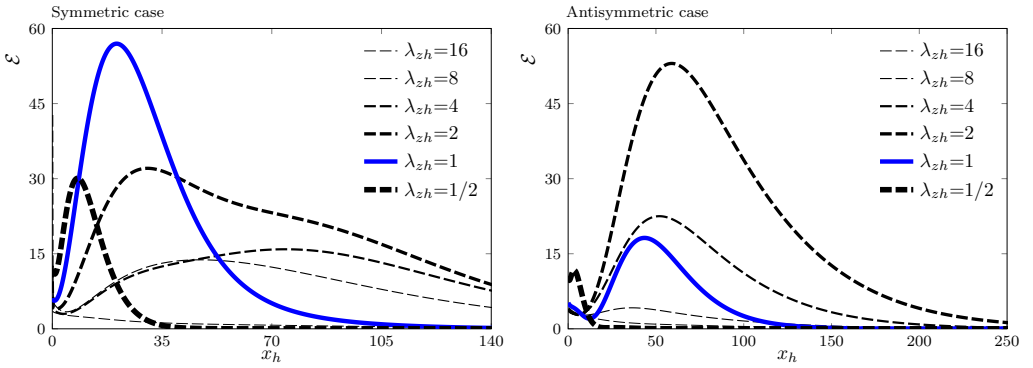

Figure 15: Effect of λ_{zh} on the downstream evolution of total energy $\mathcal{E}$ for the symmetric-gust case (left) and the anti-symmetric-gust case (right).

region of pressure-driven incompressible plane channel flows, as steps towards the full comprehension of laminar to turbulent transition in confined flows. The focus is in a Reynolds-number range where experimental evidence has documented the occurrence of intense transient growth, despite the flow being stable when studied through classical stability analysis.

The mathematical approach is based on the method of matched asymptotic expansions and on the assumption of high Reynolds number, and is pertinent to naturally present and physically realisable free-stream perturbations. The low-frequency assumption has been motivated by the ample evidence that these disturbances amplify the most in open free-stream boundary layers to form transition-triggering Klebanoff modes. This framework has allowed for a precise analytical description of the base flow and of realistic vortical perturbations that can be created in a laboratory set-up at the channel mouth. The effects of the channel confinement, the streamwise pressure gradient, and the viscous/inviscid interplay have been revealed through the analysis. We have shown how the amplitude of the initial disturbance is not arbitrary, but is instead uniquely related to, and amplified from, the one of the oncoming free-stream perturbation. The wall-normal transpiration effect of the perturbation from the boundary layer is the source of the second-order perturbations in the inviscid core. Furthermore, the composite velocity profiles of both the base flow and the disturbance flow have served the purpose of rigorous initial conditions for the parabolic base-flow boundary-layer equations and the boundary-region perturbation equations. The latter equations have been cast in a numerically-efficient vertical-velocity and vertical-vorticity formulation containing extra terms with respect to the classical Orr-Sommerfeld-Squire equations because of the non-negligible influence of nonparallel effects.

The base-flow quantities agree with results from direct numerical simulations and experiments, and we have found that monitoring the second derivative of the base flow at the channel centerline is the most conservative method for quantifying the length of the entrance region. A complete parametric study has been carried out on the perturbation flow where the base flow departs significantly from the Blasius self-similar form and is thus fully influenced by the streamwise pressure gradient, the wall-normal velocity component and the confinement of the channel walls. In the proximity of the channel mouth where the base-flow pressure gradient plays a minimal role, the disturbance flow is most dominant within the boundary layers attached to the channel walls because of the shear-driven amplifying effect responsible for the formation of the streamwise-elongated streaks. As the wall-confinement becomes paramount the viscous disturbances permeate

the whole channel, although the base flow is still mostly inviscid in the core. For all the tested cases, the intense transient growth and the subsequent decay are always detected in the entrance region, i.e., where the base flow has not reached the parabolic Poiseuille profile. A pressing issue is thus to test the effect of nonlinearity on this result, that is, to verify whether nonlinear vortices may persist downstream of the entrance region. We further find that symmetrical disturbances exhibit a more significant growth than anti-symmetrical disturbances for the same frequency and wavelengths. The latter can linger for several channel heights downstream before displaying the transient growth, a unique feature that has never been detected in open free-stream boundary layers. The disturbance growth is intensified as the frequency decreases and the bulk Reynolds number and the wall-normal wavelength increase. The spanwise wavelengths that cause the most intense downstream growth are computed.

We plan to extend our work to include a full spectrum of oncoming disturbances and to relax the assumption of small amplitude to study the nonlinearly evolving flow and its secondary instability. A next step will be to provide a robust inlet flow field for direct numerical simulations with the aim of investigating the full-fledged transitional flow. A central objective is certainly to predict the transition location as a function of the characteristics of the oncoming vortical flow at the channel mouth.

Acknowledgements

The authors would like to thank the A*STAR-Sheffield Research Attachment Programme and the University of Sheffield for funding this research. We also indebted to Dr Vinh Nguyen from the Institute of High Performance Computing in Singapore and to Professor Xuesong Wu from Imperial College London for the interesting discussions about our work.

Declaration of interests

The authors report no conflict of interest.

REFERENCES

Alizard, F., Cadiou, A., Le Penven, L., Di Pierro, B. & Buffat, M. 2018 Space-time dynamics of optimal wavepackets for streaks in a channel entrance flow. *J. Fluid Mech.* **844**, 669–706.

Andersson, P., Berggren, M. & Henningson, D.S. 1999 Optimal disturbances and bypass transition in boundary layers. *Phys. Fluids* **11** (1), 134–150.

Asai, M. & Floryan, J.M. 2004 Certain aspects of channel entrance flow. *Phys. Fluids* **16** (4), 1160–1163.

Beavers, G.S., Sparrow, E.M. & Magnuson, R.A. 1970 Experiments on hydrodynamically developing flow in rectangular ducts of arbitrary aspect ratio. *Int. J. Heat Transfer* **13**, 689–702.

Bodoia, J.R. & Osterle, J.F. 1962 Finite difference analysis of plane Poiseuille and Couette flow developments. *App. Sc. Res.* **10** (1), 265–276.

Borodulin, V.I., Ivanov, A.V., Kachanov, Y.S. & Roschektayev, A.P. 2021*a* Distributed vortex receptivity of a swept-wing boundary layer. Part 1. Efficient excitation of CF modes. *J. Fluid Mech.* **908** (A14).

Borodulin, V.I., Ivanov, A.V., Kachanov, Y.S. & Roschektayev, A.P. 2021*b* Distributed vortex receptivity of a swept-wing boundary layer. Part 2. Receptivity characteristics. *J. Fluid Mech.* **908** (A15).

Brandt, L., Schlatter, P. & Henningson, D.S. 2004 Transition in boundary layers subject to free-stream turbulence. *J. Fluid Mech.* **517**, 167–198.

Buffat, M., Le Penven, L., Cadiou, A. & Montagnier, J. 2014 DNS of bypass transition in entrance channel flow induced by boundary layer interaction. *Eur. J. Mech. - B/Fluids* **43**, 1–13.

Carlson, D.R., Widnall, S.E. & Peeters, M.F. 1982 A flow-visualization study of transition in plane Poiseuille flow. *J. Fluid Mech.* **121**, 487–505.

Cebeci, T. 2002 *Convective Heat Transfer*. Springer-Verlag, Berlin Heidelberg.

Chen, T.S. & Sparrow, E.M. 1967 Stability of the developing laminar flow in a parallel-plate channel. *J. Fluid Mech.* **30 (2)**, 209–224.

Collins, M. & Schowalter, W.R. 1962 Laminar flow in the inlet region of a straight channel. *Phys. Fluids* **5**, 1122–1124.

Davies, S.J. & White, C.M. 1928 An experimental study of the flow of water in pipes of rectangular section. *Proc. Royal Soc. London* **119** (781), 92–107.

Dietz, A.J. 1999 Local boundary-layer receptivity to a convected free-stream disturbance. *J. Fluid Mech.* **378**, 291–317.

Drazin, P.G. & Reid, W.H. 2004 *Hydrodynamic stability*. Cambridge Mathematical Library.

Dryden, H.L. 1936 Air flow in the boundary layer near a plate. *NACA Rep.* **562**.

Dryden, H.L. 1955 Transition from laminar to turbulent flow at subsonic and supersonic speeds. *Conference on High-Speed Aeronautics, 41, Polytechnic of Brooklyn, New York* .

Duck, P.W. 2005 Transient growth in developing plane and Hagen Poiseuille flow. *Proc. Royal Soc. London. Series A.* **461**, 1311–1333.

Garg, V.K. & Gupta, S.C. 1981*a* Nonparallel effects on the stability of developing flow in a channel. *Phys. Fluids* **24(9)**, 1752–1754.

Garg, V.K. & Gupta, S.C. 1981*b* Stability of the nonparallel developing flow in a channel. *Comp. Meth. Appl. Mech. Eng.* **29**, 259–269.

Goldstein, M.E. 1978 Unsteady vortical and entropic distortions of potential flows round arbitrary obstacles. *J. Fluid Mech.* **89**, 433–468.

Goldstein, M.E. 1983 The evolution of Tollmien-Schlichting waves near a leading edge. *J. Fluid Mech.* **127**, 59–81.

Goldstein, M.E. 1985 Scattering of acoustic waves into Tollmien-Schlichting waves by small streamwise variations in surface geometry. *J. Fluid Mech.* **154**, 509–529.

Grosch, C.E. & Salwen, H. 1978 The continuous spectrum of the Orr-Sommerfeld equation. Part 1. The spectrum and the eigenfunctions. *J. Fluid Mech.* **87**, 33–54.

Gupta, S.C. & Garg, V.K. 1981*a* Linear spatial stability of developing flow in a parallel plate channel. *J. Appl. Mech.* **48**, 192–194.

Gupta, S.C. & Garg, V.K. 1981*b* Stability of developing flow in a two-dimensional channel - symmetric vs. antisymmetric disturbances. *Comp. Meth. Appl. Mech. Eng.* **27**, 363–368.

Gustavsson, L.H. 1991 Energy growth of three-dimensional disturbances in plane Poiseuille flow. *J. Fluid Mech.* **224**, 241.

Hahneman, E., Freeman, J.C. & Finston, M. 1948 Stability of boundary layers and of flow in entrance section of a channel. *J. Aero. Sc.* **15** (8), 493–496.

Hunt, J.C.R. 1973 A theory of turbulent flow round two-dimensional bluff bodies. *J. Fluid Mech.* **61** (04), 625–706.

Jacobs, R.G. & Durbin, P.A. 2001 Simulation of bypass transition. *J. Fluid Mech.* **428**, 185–212.

Kao, T.W. & Park, C. 1970 Experimental investigations of the stability of channel flows. part 1. flow of a single liquid in a rectangular channel. *J. Fluid Mech.* **43** (1), 145–164.

Kemp, N. 1951 The laminar three-dimensional boundary layer and a study of the flow past a side edge. *MSc Thesis, Cornell University* .

Kendall, J.M. 1991 Studies on laminar boundary layer receptivity to free-stream turbulence near a leading edge. *In Boundary Layer Stability and Transition to Turbulence (ed. D.C. Reda, H.L. Reed & R. Kobayashi). ASME FED* **114**, 23–30.

Kim, J., Moin, P. & Moser, R. 1987 Turbulence statistics in fully developed channel flow at low Reynolds number. *J. Fluid Mech.* **177**, 133–166.

Klebanoff, P.S. 1971 Effect of free-stream turbulence on a laminar boundary layer. *Bull. Am. Phys. Soc.* **16**, 1323.

Leib, S.J., Wundrow, D.W. & Goldstein, M.E. 1999 Effect of free-stream turbulence and other vortical disturbances on a laminar boundary layer. *J. Fluid Mech.* **380**, 169–203.

Luchini, P. 1996 Reynolds-number-independent instability of the boundary layer over a flat surface. *J. Fluid Mech.* **327**, 101–115.

Luchini, P. 2000 Reynolds-number-independent instability of the boundary layer over a flat surface: optimal perturbations. *J. Fluid Mech.* **404**, 289–309.

Marensi, E., Ricco, P. & Wu, X. 2017 Nonlinear unsteady streaks engendered by the interaction of free-stream vorticity with a compressible boundary layer. *J. Fluid Mech.* **817**, 80–121.

Matsubara, M. & Alfredsson, P.H. 2001 Disturbance growth in boundary layers subjected to free-stream turbulence. *J. Fluid Mech.* **430**, 149–168.

Morkovin, M.V. 1984 Bypass transition to turbulence and research desiderata. *NASA CP-2386 Transition in Turbines* pp. 161–204.

Nishioka, M. & Asai, M. 1985 Some observations of the subcritical transition in plane Poiseuille flow. *J. Fluid Mech.* **150**, 441–450.

Nishioka, M., Iida, S. & Ichikawa, Y. 1975 An experimental investigation of the stability of plane Poiseuille flow. *J. Fluid Mech.* **72**, 731–751.

Orszag, S.A. 1971 Accurate solution of the Orr-Sommerfeld stability equation. *J. Fluid Mech.* **50**, 689–703.

Patel, V.C. & Head, M.R. 1969 Some observations on skin friction and velocity profiles in fully developed pipe and channel flows. *J. Fluid Mech.* **38** (1), 181–201.

Reed, H.L., Reshotko, E. & Saric, W.S. 2015 Receptivity: The inspiration of Mark Morkovin. In *45th AIAA Fluid Dynamics Conference*, p. 2471.

Reynolds, O. 1883 An experimental investigation of the circumstances which determine whether the motion of water shall be direct or sinuous, and of the law of resistance in parallel channels. *Phil. Trans. R. Soc.* **35** (224-226), 84–99.

Ricco, P. 2009 The pre-transitional Klebanoff modes and other boundary layer disturbances induced by small-wavelength free-stream vorticity. *J. Fluid Mech.* **638**, 267–303.

Ricco, P., Luo, J. & Wu, X. 2011 Evolution and instability of unsteady nonlinear streaks generated by free-stream vortical disturbances. *J. Fluid Mech.* **677**, 1–38.

Ricco, P., Walsh, E.J., Brighenti, F. & McEligot, D.M. 2016 Growth of boundary-layer streaks due to free-stream turbulence. *Int. J. Heat Fluid Flow* **61**, 272–283.

Ruban, A.I. 1984 On Tollmien-Schlichting wave generation by sound. *Izv. Akad. Nauk SSSR Mekh. Zhid. Gaza* **5**, 44.

Ruban, A.I. 1985 On the generation of Tollmien-Schlichting waves by sound. *Fluid Dyn.* **25(2)**, 213–221.

Rubin, S.G., Khosla, P.K. & Saari, S. 1977 Laminar flow in rectangular channels. *Computers and Fluids* **5**, 151–173.

Schlichting, H. 1934 Laminar channel entrance flow. *Z. Angew. Math. Mech.* **14**, 368–373.

Schmid, P.J. & Henningson, D.S. 2001 *Stability and Transition in Shear Flows*. Applied Mathematical Sciences, Springer, Vol. 142).

Smith, F.T. & Bodonyi, R.J. 1980 On the stability of the developing flow in a channel or circular pipe. *Quart. J. Mech. Appl. Math.* **33** (3), 293–320.

Sparrow, E.M., Hixon, C.W. & Shavit, G. 1967 Experiments on laminar flow development in rectangular ducts. *J. Basic Eng.* **89**, 116–124.

Sparrow, E.M., Lin, S.H. & Lundgren, T.S. 1964 Flow development in the hydrodynamic entrance region of tubes and ducts. *Phys. Fluids* **7** (3), 338–347.

Taylor, G.I. 1939 Some recent developments in the study of turbulence. *Fifth Intl. Congr. for Appl. Mech.* pp. 294–310.

Van Dyke, M. 1969 Entry flow in a channel. *J. Fluid Mech.* **44**, 813–823.

Westin, K.J.A., Boiko, A.V., Klingmann, B.G.B., Kozlov, V.V. & Alfredsson, P.H. 1994 Experiments in a boundary layer subjected to free stream turbulence. Part 1. Boundary layer structure and receptivity. *J. Fluid Mech.* **281**, 193–218.

Wilson, S.D.R. 1970 Entry flow in a channel. Part 2. *J. Fluid Mech.* **46**, 787–799.

Wu, X. 2001 Receptivity of boundary layers with distributed roughness to vortical and acoustic disturbances: A second-order asymptotic theory and comparison with experiments. *J. Fluid Mech.* **431**, 91–133.

Wu, X., Moin, P., Adrian, R.J. & Baltzer, J.R. 2015 Osborne Reynolds pipe flow: direct

simulation from laminar through gradual transition to fully developed turbulence. *PNAS* **112** (26), 7920–7924.

Wundrow, D.W. & Goldstein, M.E. 2001 Effect on a laminar boundary layer of small-amplitude streamwise vorticity in the upstream flow. *J. Fluid Mech.* **426**, 229–262.

Xu, D., Liu, J. & Wu, X. 2020 Görtler vortices and streaks in boundary layer subject to pressure gradient: excitation by free stream vortical disturbances, nonlinear evolution and secondary instability. *J. Fluid Mech.* **900** (A15).

Zanoun, E.-S., Kito, M. & Egbers, C. 2009 A study on flow transition and development in circular and rectangular ducts. *J. Fluids Eng.* **131** (6), 061204.

Zhang, Y., Zaki, T., Sherwin, S. & Wu, X. 2011 Nonlinear response of a laminar boundary layer to isotropic and spanwise localized free-stream turbulence. In *The 6th AIAA Theoretical Fluid Mechanics Conference*, , vol. 3292.

Entrainment and growth of vortical disturbances in the channel-entrance region - supplementary material

Pierre Ricco[1]† **and Claudia Alvarenga**[1,2]

[1]Department of Mechanical Engineering, The University of Sheffield, S1 3JD Sheffield, United Kingdom

[2]Department of Fluid Dynamics, A*Star Institute of High Performance Computing, Singapore

(Received xx; revised xx; accepted xx)

This supplementary material presents further results that are used in the main paper.

S1. Base flow in regions I and II

According to the method of matched asymptotic expansions, the composite solution reads

$$\overline{\mathbf{U}} = \overline{\mathbf{U}}_{in} + \overline{\mathbf{U}}_{out} - \overline{\mathbf{U}}_{com}, \tag{S1.1}$$

where the subscripts *in*, *out*, and *com* stand for inner, outer, and common, respectively, and $\overline{\mathbf{U}}$ is defined in (2.8). The common part is defined as

$$\overline{\mathbf{U}}_{com} = \lim_{y\to 0} \overline{\mathbf{U}}_{out} = \lim_{\eta\to\infty} \overline{\mathbf{U}}_{in}, \tag{S1.2}$$

where, for the lower channel half,

$$\eta = y\left(\frac{R_\lambda}{2x}\right)^{1/2} = \mathcal{O}(1) \tag{S1.3}$$

is the scaled wall-normal coordinate of the inner solution. As the Reynolds number is large, the inner solution near the inlet corresponds to the Blasius flow (Wilson 1970; Rubin *et al.* 1977; Duck 2005; Buffat *et al.* 2014). It satisfies

$$F''' + FF'' = 0, \tag{S1.4}$$

where the prime indicates differentiation with respect to η. The boundary conditions for equation (S1.4) are $F(0) = 0$, $F'(0) = 0$, and $F' \to 1$ as $\eta \to \infty$. The inner base flow reads

$$\overline{U}_{in} = F', \quad \overline{V}_{in} = \frac{\eta F' - F}{(2xR_\lambda)^{1/2}}. \tag{S1.5}$$

As $R_\lambda \gg 1$, the base-flow viscous effects are negligible in the channel core near the entrance, which is consistent with the use of the boundary-layer approximation of the Navier-Stokes equations. For low and moderate bulk Reynolds numbers, Wang & Longwell (1964), Van Dyke (1969), and Morihara & Cheng (1973) concluded that the vorticity and wall-normal pressure gradients at the entrance are indeed not negligible because they result from the upstream flow influence. However, as the Reynolds number increases, the core flow is not affected by the presence of the walls at leading order. As our work focuses on cases for which the Reynolds numbers are about ten times larger

† Email address for correspondence: p.ricco@sheffield.ac.uk

than in the full Navier-Stokes study by Wang & Longwell (1964), the use of potential flow theory in the channel core and the confinement of the viscous effects near the wall are justified (Rubin *et al.* 1977). In §S2, we compare our results with those obtained via direct numerical simulations (DNS) to confirm the validity of this assumption.

In the inviscid core, the outer flow is described by an inviscid streamfunction ψ,

$$\psi(x,y) = y + R_\lambda^{-1/2}\psi_2(x,y), \tag{S1.6}$$

i.e., $\overline{U}_{out} = \partial\psi/\partial y$ and $\overline{V}_{out} = -\partial\psi/\partial x$. The leading-order term y in (S1.6) defines the uniform streamwise flow. The second-order streamfunction ψ_2 defines the flow due to the channel confinement and to the Blasius boundary layers developing on the channel walls, and satisfies

$$\nabla^2\psi_2 = 0, \tag{S1.7}$$

subject to

$$\psi_2 = 0 \qquad \text{at} \qquad y = 0, 2h, x < 0, \tag{S1.8a}$$

$$\psi_2 = \pm\beta\sqrt{2x} \qquad \text{at} \qquad y = 0 \ (-\text{ sign}),\ 2h \ (+\text{ sign}), x > 0, \tag{S1.8b}$$

where $\beta = \lim_{\eta\to\infty}(\eta - F) = 1.217\ldots$ The boundary conditions (S1.8a) is obtained as follows. The base flow is uniform and streamwise only as $x \to -\infty$ and, as it is not influenced by the presence of the channel walls, no wall-normal base-flow velocity occurs as $x \to -\infty$. Also, no wall-normal base-flow velocity occurs along the horizontal lines $y = 0, 2h$ for $x < 0$ because there is no preferential wall-normal flow direction as the base flow approaches the channel walls. Therefore, $\overline{V}_{out} = 0$ at $y = 0, 2h$ for $x < 0$, i.e., $\partial\psi/\partial x = \partial\psi_2/\partial x = 0$. As we choose $\psi_2 = 0$ as $x \to -\infty$, by integrating $\partial\psi_2/\partial x = 0$ from $x \to -\infty$ for $y = 0, 2h$, it follows that $\psi_2 = 0$ along $y = 0, 2h$ for $x < 0$. The boundary conditions (S1.8b) are obtained by asymptotic matching, i.e., the wall-normal component of the outer velocity must match the outer limit of the base-flow wall-normal velocity of the boundary layer. For the lower-half boundary layer,

$$\overline{V}_{com} = \lim_{y\to 0}\overline{V}_{out} = -\frac{1}{R_\lambda^{1/2}}\frac{\partial\psi_2}{\partial x}\bigg|_{y=0} = \lim_{\eta\to\infty}\overline{V}_{in} = \lim_{\eta\to\infty}\frac{\eta F' - F}{(2xR_\lambda)^{1/2}} = \frac{\beta}{(2xR_\lambda)^{1/2}}. \tag{S1.9}$$

It follows that

$$\psi_2(x) = -\beta\int(2x)^{-1/2}\mathrm{d}x = -\beta\sqrt{2x}, \tag{S1.10}$$

at $y = 0$ for $x > 0$. The condition $\psi_2(x) = \beta\sqrt{2x}$ at $y = 2h$ in (S1.8b) follows from the antisymmetry of the wall-normal velocity. The solution to (S1.7) together with the boundary conditions (S1.8) is found by separation of variables. There exists a full analogy with a heat conduction problem and therefore we refer to page 166 in Carslaw & Jaeger (1959). The solution reads

$$\begin{aligned}\psi_2(x,y) = &\frac{1}{4h}\sin\left(\frac{\pi y}{2h}\right)\int_0^\infty \frac{-\beta\sqrt{2\sigma}\mathrm{d}\sigma}{\cosh[\pi(x-\sigma)/2h] - \cos(\pi y/2h)} + \\ &\frac{1}{4h}\sin\left(\frac{\pi y}{2h}\right)\int_0^\infty \frac{\beta\sqrt{2\sigma}\mathrm{d}\sigma}{\cosh[\pi(x-\sigma)/2h] + \cos(\pi y/2h)}.\end{aligned} \tag{S1.11}$$

The velocity components in the lower channel half read

$$\overline{U}_{out} = \frac{\partial \psi}{\partial y} = 1 + R_\lambda^{-1/2} \frac{\pi}{2h^2} \left\{ \cos\left(\frac{\pi y}{h}\right) \int_0^\infty \frac{-\beta\sqrt{2\sigma}\mathrm{d}\sigma}{\cosh\left[\pi\left(x-\sigma\right)/h\right] - \cos\left(\pi y/h\right)} + \sin^2\left(\frac{\pi y}{h}\right) \int_0^\infty \frac{\beta\sqrt{2\sigma}\mathrm{d}\sigma}{\left\{\cosh\left[\pi\left(x-\sigma\right)/h\right] - \cos\left(\pi y/h\right)\right\}^2} \right\}, \tag{S1.12}$$

$$\overline{V}_{out} = -\frac{\partial \psi}{\partial x} = -R_\lambda^{-1/2} \frac{\pi}{2h^2} \sin\left(\frac{\pi y}{h}\right) \int_0^\infty \frac{\sinh\left[\pi(x-\sigma)/h\right] \beta\sqrt{2\sigma}\mathrm{d}\sigma}{\left\{\cosh\left[\pi\left(x-\sigma\right)/h\right] - \cos\left(\pi y/h\right)\right\}^2}. \tag{S1.13}$$

The integrals in (S1.11), (S1.12) and (S1.13) are computed using the Cavalieri-Simpson rule. The computation of (S1.11) is validated by numerically solving (S1.7) with (S1.8) by use of the Gauss-Seidel method.

The common part of the wall-normal velocity is computed in (S1.9) and the common part of the streamwise velocity in the lower channel half is

$$\overline{U}_{com} = \lim_{y\to 0} \overline{U}_{out} = \lim_{\eta\to\infty} \overline{U}_{in} = 1 + R_\lambda^{-1/2} \frac{\pi}{2h^2} \int_0^\infty \frac{-\beta\sqrt{2\sigma}\mathrm{d}\sigma}{\cosh\left[\pi\left(x-\sigma\right)/h\right] - 1}. \tag{S1.14}$$

The composite solution of the streamwise velocity in the lower channel half is

$$U(x,y) = \overline{U} = F'(\eta(x,y)) + R_\lambda^{-1/2} \frac{\pi}{2h^2} \left\{ \cos\left(\frac{\pi y}{h}\right) \int_0^\infty \frac{-\beta\sqrt{2\sigma}\mathrm{d}\sigma}{\cosh\left[\pi\left(x-\sigma\right)/h\right] - \cos\left(\pi y/h\right)} + \sin^2\left(\frac{\pi y}{h}\right) \int_0^\infty \frac{\beta\sqrt{2\sigma}\mathrm{d}\sigma}{\left\{\cosh\left[\pi\left(x-\sigma\right)/h\right] - \cos\left(\pi y/h\right)\right\}^2} \right\} - R_\lambda^{-1/2} \frac{\pi}{2h^2} \int_0^\infty \frac{-\beta\sqrt{2\sigma}\mathrm{d}\sigma}{\cosh\left[\pi\left(x-\sigma\right)/h\right] - 1}. \tag{S1.15}$$

The streamwise velocity in the upper channel half is symmetric with respect to the centreline. In the composite solution (S1.15), the $\mathcal{O}\left(R_\lambda^{-1/2}\right)$ term in the boundary layer, driven by the $\mathcal{O}\left(R_\lambda^{-1/2}\right)$ term in the last line of (S1.15), is not considered, and therefore the composite solution (S1.15) is of leading-order accuracy and not accurate up to $\mathcal{O}\left(R_\lambda^{-1/2}\right)$.

The composite solution of the wall-normal velocity V, defined in (2.8), in the lower channel half is

$$V(x,y) = k_x^{-1}\overline{V} = \frac{\eta F'(\eta(x,y)) - F(\eta(x,y))}{k_x \left(2xR_\lambda\right)^{1/2}} - R_\lambda^{-1/2} \frac{\pi}{2h^2 k_x} \sin\left(\frac{\pi y}{h}\right) \int_0^\infty \frac{\sinh\left[\pi(x-\sigma)/h\right] \beta\sqrt{2\sigma}\mathrm{d}\sigma}{\left\{\cosh\left[\pi\left(x-\sigma\right)/h\right] - \cos\left(\pi y/h\right)\right\}^2} - \frac{\beta}{k_x \left(2xR_\lambda\right)^{1/2}}. \tag{S1.16}$$

The wall-normal velocity in the upper channel half is antisymmetric with respect to the centreline.

Figure S1 shows the inner and outer solutions, the common part, and the composite solution of the base-flow velocity components for $R_\lambda = 500$ and 2000 at $x = 0.05$. The

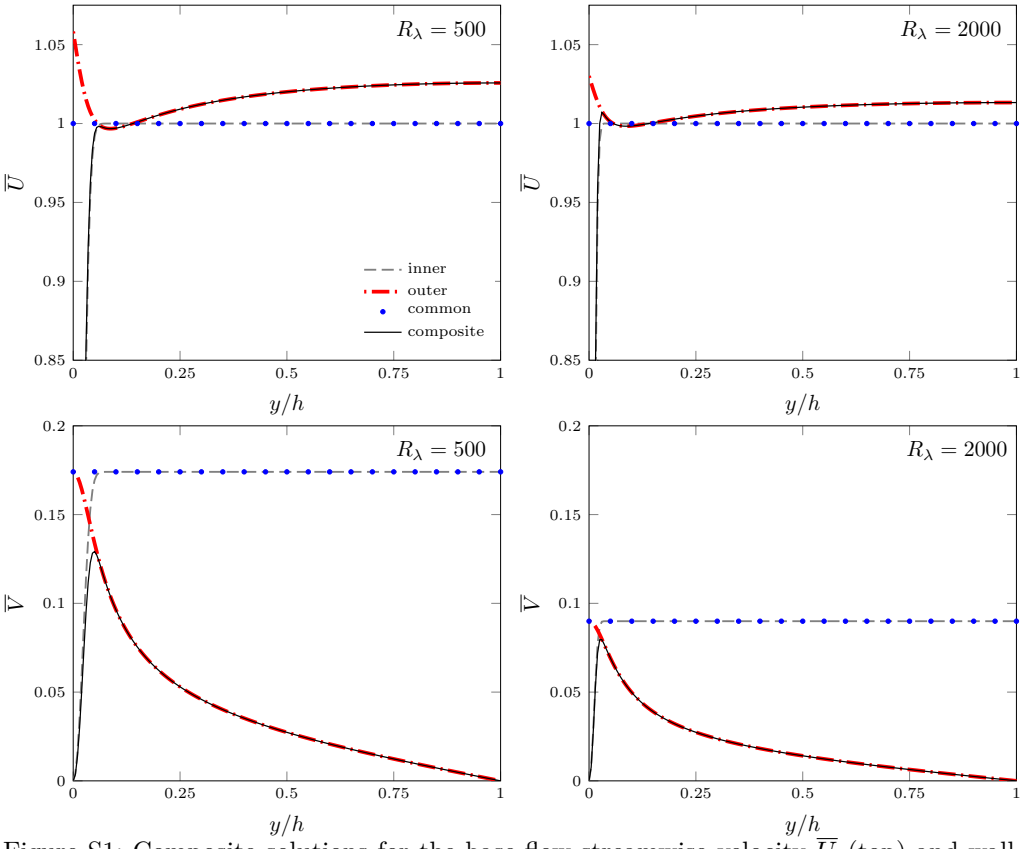

Figure S1: Composite solutions for the base-flow streamwise velocity $\overline{U}$ (top) and wall-normal velocity $\overline{V}$ (bottom) at $x = 0.05$ for two Reynolds numbers.

composite base-flow streamwise velocity, depicted in the top graphs of figure S1, agrees well with the inner Blasius solution across the channel height as the acceleration in the channel core is still small at this x location. The increase of inviscid streamwise velocity balances the decrease within the viscous region to conserve the mass flow rate. The displacement effect of the Blasius boundary layers, given by (S1.9), causes a small streamwise pressure gradient related to the dependence of the displacement streamfunction ψ_2 on the x coordinate, which is negligible at leading order in the near-wall viscous regions. This pressure-gradient effect is weaker than in the case by Xu *et al.* (2020), where the pressure gradient is more intense and non-uniform at leading order from the proximity of the confined region because induced by a converging or divergent channel. In our case, the pressure gradient instead produces a leading-order effect further downstream in region V. The inviscid streamwise velocity is larger than unity near the wall because it accelerates along x to conserve the mass flow rate as the wall-normal velocity decreases from its boundary-layer blowing value as the centreline is approached. This acceleration gives rise to the local near-wall peak in the $\overline{U}$ profile, also reported in Sparrow *et al.* (1964), Panton (2013), and Alizard *et al.* (2018). The peak occurs because the inviscid streamwise velocity is larger than the viscous streamwise velocity deficit of the boundary layer.

The base-flow wall-normal velocity, shown in the bottom graphs of figure S1, agrees well with the viscous solution only in the proximity of the wall, while the two fail to overlap

in the inviscid core, where the composite profile coincides with the outer solution. The composite solution shows a distinct peak located near the wall. As the Reynolds number increases and the viscous effects become more confined near the surface, the peak moves closer to the wall, while it decreases in amplitude and approaches the outer value more closely. The velocity is not exactly zero at the wall. This small slip velocity decreases while the Reynolds number increases as $\mathcal{O}\left(R_\lambda^{-1/2}\right)$ and induces a viscous layer at the next order, which we do not compute.

S2. Base flow in regions V and VI

The inset of figure S2 (top) shows the centreline velocity $\overline{U}_{\rm cen} = \overline{U}(x, y = h)$ computed through the inviscid solution (S1.12) (dash-dotted line) and the boundary-layer equations (2.11)-(2.10) (solid line). The inviscid solution is not zero in a small region upstream of the channel mouth as $\overline{U}_{\rm cen}$ matches the uniform velocity as $x \to -\infty$. The velocity increases as the channel entrance is approached because of the pressure gradient due to the channel confinement. Inside the channel and near the entrance, the centreline velocity $\overline{U}_{\rm cen}$ can be approximated well by the inviscid solution in an overlap region, as evidenced by the inviscid and the viscous solutions showing excellent agreement. However, as the streamfunction formulation in §S1 does not take into account the viscous effects or the base-flow pressure gradient at leading order, the agreement between the inviscid velocity and the viscous velocity computed via the boundary-layer equations (2.11)-(2.10) inevitably deteriorates downstream, where the base-flow pressure gradient is fully influential. The viscous $\overline{U}_{\rm cen}$ then becomes smaller than the inviscid $\overline{U}_{\rm cen}$ because in the former case the core flow is less restricted by the boundary layers over the channel walls as these grow less than in the latter case because they are influenced by the favourable base-flow pressure gradient. The viscous solution is not valid in the very proximity of $x = 0$ because the flow cannot be described by the boundary-layer approximation. Therefore, in order to start the downstream marching procedure, the initial position is selected to be in the range where the inviscid and viscous profiles overlap, the extent of which depends on the Reynolds number. As the Reynolds number increases, this matching region becomes larger as the channel confinement and the pressure gradient become less important.

The base-flow streamwise and wall-normal velocity profiles across the channel are shown in figure S2 for various streamwise positions. The small-x asymptotic profiles (S1.1) are also shown (dashed lines). The flow field approaches the fully-developed regime as it develops downstream: the base-flow streamwise velocity evolves to the parabolic Poiseuille profile, while the wall-normal velocity decreases to zero.

The base-flow streamwise velocity is shown in figure S3 as a function of the streamwise position at various y locations and is compared with data from the literature. There is excellent agreement with the data by Alizard *et al.* (2018) (empty squares) obtained by DNS of the full Navier-Stokes equations, thereby validating our boundary-layer approximation even in the proximity of the channel mouth. The match with the boundary-layer computations by Bodoia & Osterle (1962) (white circles) and the series solution by Sparrow *et al.* (1964) (black circles) is also very good, although near the entrance a slight disagreement is observed with Sparrow *et al.* (1964)'s centreline data and with Bodoia & Osterle (1962)'s data near the wall. The mismatch with the latter could be due to an insufficient numerical resolution due to the high near-wall velocity gradients in the proximity of the channel mouth. The data point by Schlichting (1934) (blue + symbol at $x/(h^2 R_\lambda) = 0.016$), computed by a composite solution of a viscous-flow series and an inviscid-core solution, shows poor agreement because, as pointed out by Bodoia &

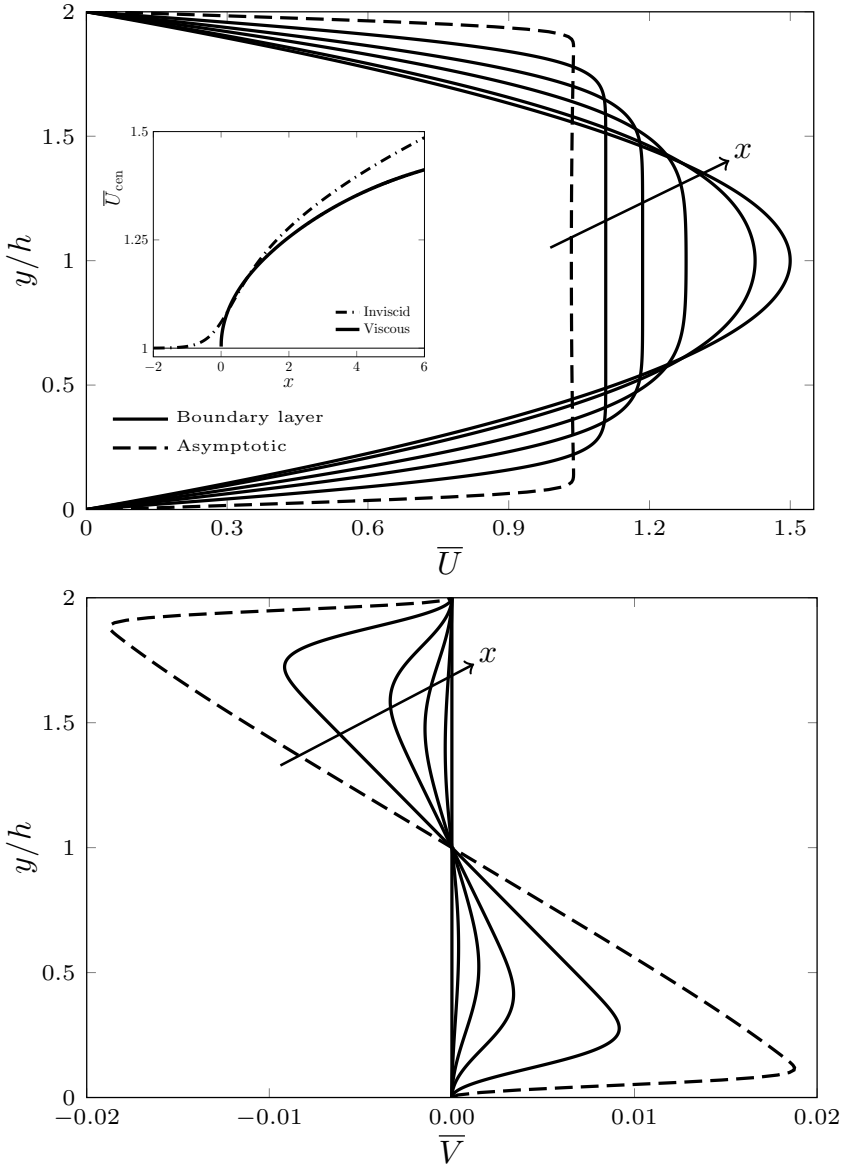

Figure S2: Streamwise (top) and wall-normal (bottom) base-flow velocity profiles. The solid lines denote the solutions at $x/(h^2R_\lambda) = 0.003, 0.012, 0.03, 0.08, 0.4$ obtained by numerically solving the boundary-layer equations (2.11)-(2.10). The dashed lines show the composite solution of the streamwise velocity (S1.15) (top) and of the wall-normal velocity (S1.16) (bottom) at $x/(h^2R_\lambda) = 0.0004$. Inset of top graph: centreline base-flow velocity $\overline{U}_{\rm cen}$ as a function of the streamwise coordinate for $R_\lambda = 75$. The dash-dotted line represents the inviscid solution (S1.15) and the solid line indicates the numerical solution of (2.11)-(2.10).

Osterle (1962), the second derivative of the streamwise velocity, neglected by Schlichting (1934) in the outer solution, has a non-zero value. Collins & Schowalter (1962) improved Schlichting (1934)'s theory by including more terms in the approximation to obtain a

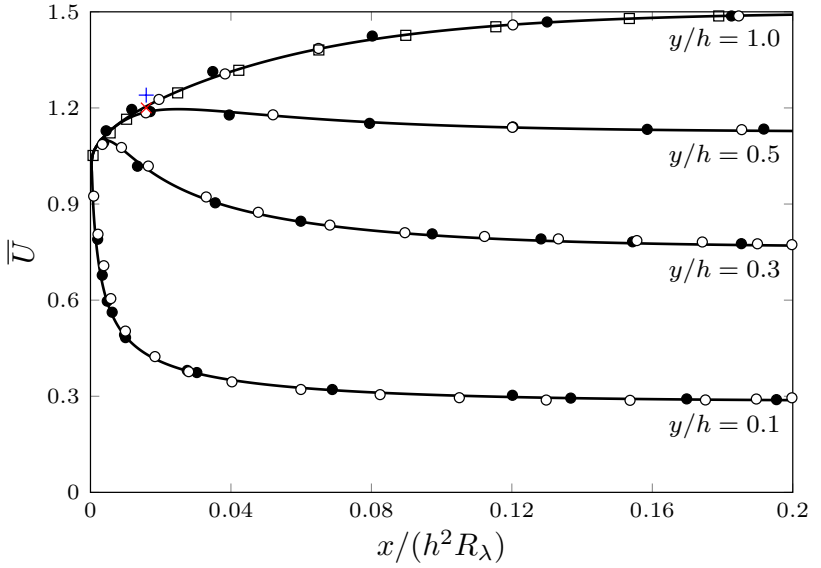

Figure S3: Base-flow streamwise velocity $\overline{U}$ at different y/h locations as a function of the streamwise coordinate, computed by numerically solving the boundary-layer equations (2.11)-(2.10) (solid lines). Symbols: DNS data Alizard *et al.* (2018) (empty squares), boundary-layer data by Bodoia & Osterle (1962) (white circles), series solution by Sparrow *et al.* (1964) (black circles), composite solution by Schlichting (1934) (blue + symbol), and improved composite solution by Collins & Schowalter (1962) (red × symbol).

more accurate result, which matches ours very well (red × symbol at $x/(h^2R_\lambda) = 0.016$).

The downstream adjustment of the pressure gradient can be monitored through the correction pressure function

$$\mathcal{K}\left(\frac{x}{h^2R_\lambda}\right) = \frac{|\Delta\overline{P}^*|}{\rho^* U_\infty^{*2}} - \frac{3\nu^* x^*}{h^{*2}U_\infty^*} = |\Delta\overline{P}| - \frac{3x}{h^2R_\lambda}, \tag{S2.1}$$

which measures the deviation of the base-flow pressure, defined in (2.8), from the fully-developed Poiseuille value. Our computed fully-developed value is $\mathcal{K}_\infty = \lim_{x\to\infty}\mathcal{K}(x) = 0.336$. As shown in figure S4 and consistently with the discussion about the computation of $\overline{U}_{\rm cen}$, the $\mathcal{K}_\infty$ value computed by Schlichting (1934) (blue + symbol) does not match any other, while Collins & Schowalter (1962)'s value (red × symbol) is in excellent agreement with ours and with Bodoia & Osterle (1962)'s (white points), while being only slightly lower than Lundgren *et al.* (1964)'s (orange square). Our data perfectly match Bodoia & Osterle (1962)'s points and are only marginally higher than Sparrow *et al.* (1964)'s (black circles). The comparison with the experimental data by Beavers *et al.* (1970) is also satisfactory (white circles with + symbol), especially when the fully-developed value is approached. This agreement is expected as, arguably, the uncertainty is larger near the channel mouth where the pressure and velocity gradients are largest. Their aspect ratio of 51:1 is almost certainly sufficiently large as their pressure data for the channel with aspect ratio 20:1 leads to values within the experimental uncertainty. The $\mathcal{K}$ values by Asai & Floryan (2004) (white circles with × symbol), obtained from the experimental pressure data in their figure 1 measured in a channel of aspect ratio 27.6:1, are lower than the numerical data. This mismatch could be due to differences in the channel mouth, which

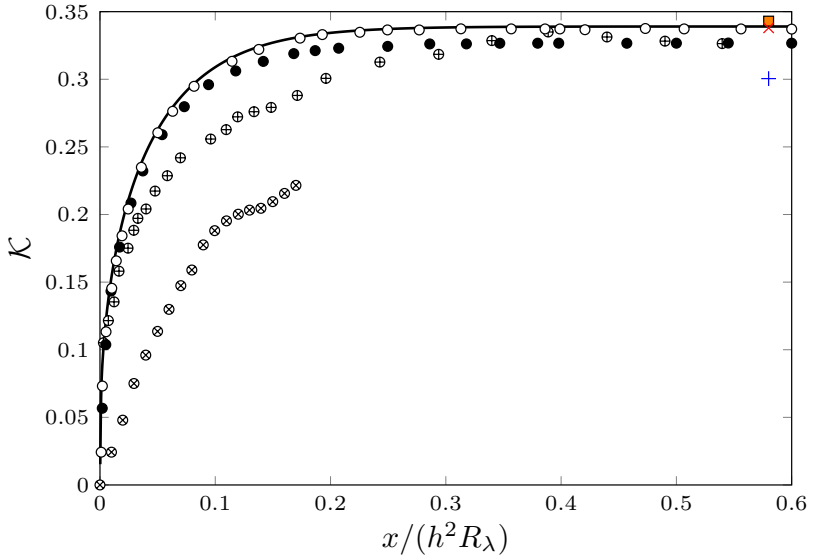

Figure S4: Correction pressure function $\mathcal{K}$, defined in (S2.1), as a function of the streamwise coordinate, computed by numerically solving the boundary-layer equations (2.11)-(2.10) (solid line). Symbols: series solution by Lundgren *et al.* (1964) (orange square), experimental data by Beavers *et al.* (1970) (white circles with + symbol) and by Asai & Floryan (2004) (white circles with × symbol). The legend for the black and white circles, the blue + symbol, and the red × symbol is the same as in figure S3.

are not described in Asai & Floryan (2004) because their focus was further downstream, near the fully-developed region. Their asymptotic value, $\mathcal{K}_\infty = 0.23$, computed by fitting their large-x formula $\mathcal{K} = \mathcal{K}_\infty + C\exp(-\xi x)$ to the experimental data (where C is a constant and ξ is an eigenvalue), is much lower than our numerical value.

We now define boundary-layer thicknesses to quantify the diffusion of the viscous effects as the flow develops downstream. They are defined as

$$\delta_k = \Delta_k \int_0^h \left[1 - \frac{\overline{U}(x,y)}{\overline{U}_{\rm cen}(x)}\right] \mathrm{d}y, \tag{S2.2}$$

where $k = h$ identifies the boundary thickness that matches the half channel height in the fully-developed downstream limit ($\Delta_h = 3$ is obtained by substituting $\delta_h = h$, $\lim_{x\to\infty}\overline{U}(x,y) = 3y(2-y/h)/2h$, and $\lim_{x\to\infty}\overline{U}_{\rm cen} = 3/2$ into (S2.2)) and $k =$ LWG,CH denotes the boundary thickness that matches the one employed by LWG99 as $x \to 0$, i.e., $\delta_{\rm LWG} = (2x/R_\lambda)^{1/2}$ ($\Delta_{\rm LWG,CH} = \beta^{-1} = 0.822$ is obtained by substituting (S1.15) into (S2.2)). Figure S5 (left) shows the boundary-layer thicknesses as functions of the streamwise coordinate. The thickness $\delta_{\rm LWG,CH}$ in our channel-flow case is thinner than the corresponding Blasius-flow $\delta_{\rm LWG}$ because of the accelerating core caused by the favourable pressure gradient.

We also quantify the entry length, i.e., the distance from the channel mouth where region V ends and the fully-developed region VI starts. The entry length is typically defined by the streamwise location where $\overline{U}_{\rm cen}$ reaches 99% of its fully-developed value. We can first use equation (23) in Durst *et al.* (2005), i.e., $x_{e,u} = 2h\left[0.4787 + (2C_{e,u}hR_\lambda)^{1.6}\right]^{1/1.6}$, where $C_{e,u} = 0.0442$. As we operate under the assumption $R_\lambda \gg 1$, Durst *et al.* (2005)'s equation reduces to $x_{e,u} = 4C_{e,u}h^2R_\lambda$, which is consistent with the scaling adopted in figure S3. We compute $C_{e,u} = 0.043$, which is within the uncertainty range provided by

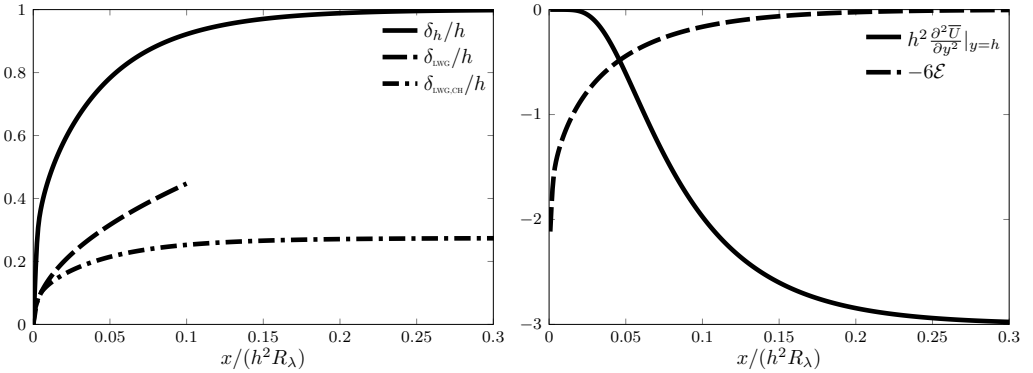

Figure S5: Left: Boundary-layer thicknesses δ_h, δ_{LWG}, and $\delta_{\text{LWG,CH}}$ as functions of the streamwise coordinate. Right: Second derivative of the streamwise velocity at the centreline and average error $\mathscr{E}$, defined in the text and measuring the deviation of the $\overline{U}$ profile from the Poiseuille solution, as functions of the streamwise coordinate.

Durst *et al.* (2005). We also quantify the entrance region as $x_{e,pres} = 4C_{e,pres}h^2R_\lambda$, i.e., the streamwise distance from the channel mouth where $\mathcal{K} = 0.99\mathcal{K}_\infty$, that is, where the pressure gradient has reached its fully developed constant value. We compute $C_{e,pres} = 0.054$.

Crabtree, Küchemann, and Sowerby on page 440 of Rosenhead (1963) remark that in a pipe entrance flow:"...the whole of the fluid across a section becomes influenced by viscosity before the parabolic distribution is reached." We can examine this statement in our case of channel flow, although they do not specify how the diffusion of viscous effects is defined mathematically. The flow development to the Poiseuille parabolic profile is already quantified by the entry length $x_{e,u}$, based on the downstream evolution of $\overline{U}_{\text{cen}}$, but we also further monitor it by an adjustment length $x_{e,pois} = 4C_{e,pois}h^2R_\lambda$, defined as the streamwise location where the average difference between the streamwise velocity and the Poiseuille velocity, i.e., $\mathscr{E}(x) = (1/h)\int_0^h |\overline{U}(x,y) - 3y(2-y/h)/2h|\mathrm{d}y$ (shown by the dashed line in figure S5, right), has decayed to 1% of $\lim_{x\to 0}\mathscr{E} = 1$. We find $C_{e,pois} = 0.038$, i.e., comparable with $C_{e,u}$. The diffusion of viscous effects can be quantified by two adjustment lengths. We first obtain $x_{e,u2} = 4C_{e,u2}h^2R_\lambda$, i.e., the downstream distance from the channel mouth where the second derivative of the streamwise velocity with respect to the wall-normal direction at the centreline, $\partial^2\overline{U}/\partial y^2|_{y=h}$ (shown by the solid line in figure S5, right), is 99% of its fully-developed value. We choose this quantity because it represents wall-normal viscous effects and the centreline is the last wall-normal location where the viscous diffusion from the wall is felt. We compute $C_{e,u2} = 0.072$. We then find $x_{e,\delta} = 4C_{e,\delta}h^2R_\lambda = 0.052$, i.e., the downstream distance from the entrance where δ_h=0.99h. Table S1 summarizes the computed entrance lengths.

We therefore find that $C_{e,u2}$, $C_{e,\delta} > C_{e,u}, C_{e,pois}$, i.e., the flow becomes viscous for the whole wall-normal extent of the channel slightly downstream from where the flow can be considered in good agreement with the Poiseuille profile. Therefore, there does not exist a distinct streamwise region along which viscous diffusion affects the whole wall-normal extent of the channel and the velocity profile has not yet developed to the parabolic profile. It remains to be verified whether this streamwise region exists in a pipe flow, as stated by Crabtree, Küchemann, and Sowerby. The adjustment length $x_{e,u2}$, based on the second wall-normal derivative of the streamwise velocity at the centreline, is the most conservative amongst the four lengths, as also visually evident in figure S5 (right).

Criterion	$\mathrm{d}\overline{P}/\mathrm{d}\overline{x}$	$\mathscr{E}$	$\overline{U}_p(y=h)$	δ_h	$\left.\frac{\partial^2\overline{U}}{\partial y^2}\right\vert_{y=h}$
Parameter	$C_{e,pres}$	$C_{e,pois}$	$C_{e,u}$	$C_{e,\delta}$	$C_{e,u2}$
	0.054	0.038	0.043	0.052	0.072
Entry length	$x_{e,pres}/(h^2R_\lambda)$	$x_{e,pois}/(h^2R_\lambda)$	$x_{e,u}/(h^2R_\lambda)$	$x_{e,\delta}/(h^2R_\lambda)$	$x_{e,u2}/(h^2R_\lambda)$
	0.216	0.152	0.172	0.208	0.288

Table S1: Entrance lengths according to definitions presented in the text.

REFERENCES

Alizard, F., Cadiou, A., Le Penven, L., Di Pierro, B. & Buffat, M. 2018 Space-time dynamics of optimal wavepackets for streaks in a channel entrance flow. *J. Fluid Mech.* **844**, 669–706.

Asai, M. & Floryan, J.M. 2004 Certain aspects of channel entrance flow. *Phys. Fluids* **16** (4), 1160–1163.

Beavers, G.S., Sparrow, E.M. & Magnuson, R.A. 1970 Experiments on hydrodynamically developing flow in rectangular ducts of arbitrary aspect ratio. *Int. J. Heat Transfer* **13**, 689–702.

Bodoia, J.R. & Osterle, J.F. 1962 Finite difference analysis of plane Poiseuille and Couette flow developments. *App. Sc. Res.* **10** (1), 265–276.

Buffat, M., Le Penven, L., Cadiou, A. & Montagnier, J. 2014 DNS of bypass transition in entrance channel flow induced by boundary layer interaction. *Eur. J. Mech. - B/Fluids* **43**, 1–13.

Carslaw, H.S. & Jaeger, J.C. 1959 *Conduction of heat in solids*. Clarendon Press.

Collins, M. & Schowalter, W.R. 1962 Laminar flow in the inlet region of a straight channel. *Phys. Fluids* **5**, 1122–1124.

Duck, P.W. 2005 Transient growth in developing plane and Hagen Poiseuille flow. *Proc. Royal Soc. London. Series A.* **461**, 1311–1333.

Durst, F., Ray, S., Ünsal, B. & Bayoumi, O.A. 2005 The development lengths of laminar pipe and channel flows. *J. Fluids Eng.* **127** (6), 1154–1160.

Lundgren, T.S., Sparrow, E.M. & Starr, J.B. 1964 Pressure drop due to the entrance region in ducts of arbitrary cross section. *Trans. ASME J. Basic Eng.* pp. 620–626.

Morihara, H. & Cheng, R.T.S. 1973 Numerical solution of the viscous flow in the entrance region of parallel plates. *J. Comp. Phys.* **11** (4), 550–572.

Panton, R. 2013 *Incompressible Flow*. Wiley-Interscience – Fourth Edition.

Rosenhead, L. 1963 *Laminar Boundary Layers*. Dover.

Rubin, S.G., Khosla, P.K. & Saari, S. 1977 Laminar flow in rectangular channels. *Computers and Fluids* **5**, 151–173.

Schlichting, H. 1934 Laminar channel entrance flow. *Z. Angew. Math. Mech.* **14**, 368–373.

Sparrow, E.M., Lin, S.H. & Lundgren, T.S. 1964 Flow development in the hydrodynamic entrance region of tubes and ducts. *Phys. Fluids* **7** (3), 338–347.

Van Dyke, M. 1969 Entry flow in a channel. *J. Fluid Mech.* **44**, 813–823.

Wang, Y.L. & Longwell, P.A. 1964 Laminar flow in the inlet section of parallel plates. *AIChE J.* **10** (3), 323–329.

Wilson, S.D.R. 1970 Entry flow in a channel. Part 2. *J. Fluid Mech.* **46**, 787–799.

Xu, D., Liu, J. & Wu, X. 2020 Görtler vortices and streaks in boundary layer subject to pressure gradient: excitation by free stream vortical disturbances, nonlinear evolution and secondary instability. *J. Fluid Mech.* **900** (A15).